

1 We thank the Reviewer for the comments and suggestions to improve our paper. We feel the changes and  
2 additions we have made have improved the paper and provide a much better manuscript for the HESS  
3 audience. We have addressed each comment individually, below:

4 **ANONYMOUS REFEREE #3**

5 **RECEIVED AND PUBLISHED: 1 SEPTEMBER 2014**

6 **Summary: This is a welcome paper that addresses the difficult problem of parameterizing urban**  
7 **canopy models for use in gridded LSM simulations. Analysis and writing are clear throughout, and I**  
8 **have only minor corrections/comments that I would ask the authors to address before final**  
9 **publication.**

10 **MINOR COMMENTS:**

11 **p.7475 line 7: "2033" should be "2003"**

12 We appreciate the reviewer's comment. The change is made.

13 **p.7476 Equation 3: Are there no street trees in the study area? In many cities the canopy cover of**  
14 **street trees—which would show up as GVF—far exceeds the impervious area associated with tree pits,**  
15 **suggesting that Eq 3 would significantly underestimate impervious area.**

16 We agree with the reviewer's comment. The assumption that the remote sensing based GVF is  
17 equivalent to impervious fraction is associated with errors induced by non-vegetated pervious areas and  
18 tree canopies that cover areas larger than underlying pervious surfaces. However, as mentioned in the  
19 manuscript the non-vegetated previous surfaces are rare and offset the impact of trees canopies over  
20 small impervious areas.

21 To address the reviewer's comment the following is **added** to the manuscript (section 3: Remotely  
22 Sensed Parameters):

23 *"We speculate that one cause that may contribute to the high accuracy of this assumption is that ISA*  
24 *overestimation, induced by non-vegetated pervious surfaces, is offset by tree canopies that cover areas*  
25 *larger than underlying pervious surfaces."*

26 **p. 7476 line 14: If ISA is defined as a continuous variable, what does it mean to have an accuracy of**  
27 **95%? Was a threshold applied to distinguish between pervious and impervious pixels?**

28 In the Noah-UCM modeling framework, each pixel consists of pervious and impervious fractions. The  
29 impervious fraction is called impervious surface area (ISA) or urban fraction. The mentioned comparison,  
30 in the current study, is based on spatial averages of ISAs over the entire study domain using the remote  
31 sensing data and a very high resolution land cover map of Los Angeles produced by McPherson et al.  
32 [2008].

33 References:

34 McPherson, E. G., Simpson, J. R., Xiao, Q., Wu, C.: Los Angeles 1-million tree canopy cover assessment,  
35 Gen. Tech. Rep. PSW-GTR-207, Albany, CA: U.S. Department of Agriculture, Forest Service, Pacific  
36 Southwest Research Station, 52 p, 2008.

37 **p. 7485 line 12: MOSID should be MODIS**

38 We appreciate the reviewer's comment. The change is made.

39 **p. 7487 line 20: Presumably the authors mean that the lookup tables over or underestimate albedo**  
40 **relative to estimates calculated using RS data. This should be stated.**

41 We agree with the reviewer's comment and **added** the following (underlined) to the manuscript (section  
42 6.2):

43 *"The Noah-UCM parameters, based on look-up tables, underestimate surface albedo values over highly*  
44 *urbanized pixels, when compared with remote sensing data (Fig. 3i and 3j)."*

45 **p. 7491 line 6: The large errors in LST estimation are one of the more interesting results of this study.**  
46 **While the authors attribute this to structural model issues that are addressed in other papers, I**  
47 **wonder how sensitive the result is to choice of forcing data. The station-based forcing used in this**  
48 **study probably fails to capture fine scale variability in 2m air temperature within the urban canopy.**  
49 **This variability could have an impact on simulated LST in an offline simulation. Could the authors**  
50 **comment on this possibility?**

51 We agree with the reviewer's comment and did further investigation on the LST underestimation  
52 problem. Guided by a study by Li and Bou-Zeid [2014], we realized that this is due to the fact that in the  
53 current Noah-UCM code, the turbulent transfer coefficient ( $C_h$ ) for the whole pixel is calculated using  
54 only momentum and thermal roughness lengths of vegetated portion, ignoring the developed surface  
55 impact on  $C_h$ . In the current resubmission, we re-ran the simulations, adopting the revised calculation of  
56 LST proposed by Li and Bou-Zeid [2014]. Using the new approach, the LST values over highly developed  
57 surfaces are significantly increased. This solves the LST underestimation problem in these areas (see  
58 revised Figs. 5 and 6). To implement the revised LST calculation, the following changes are made to the  
59 manuscript:

60 The following section is **ADDED** to the manuscript:

61 *"4.3. Improving the UCM-simulated LST*

62 *The calculation of the impervious surface temperature in the UCM version used in this study has been*  
63 *shown to be inaccurate [Li and Bou-Zeid, 2014]. This is due to the fact that the turbulent transfer*  
64 *coefficient ( $C_h$ ) for the whole pixel is calculated using only momentum and thermal roughness lengths of*  
65 *vegetated portion, ignoring the developed surface impact on  $C_h$ . Li and Bou-Zeid [2014] showed that this*  
66 *inconsistency could result in large biases in simulated LST values. In the current study, an alternative LST*  
67 *calculation, proposed by Li and Bou-Zeid [2014], is used as follows. First, a revised surface temperature of*

68 the impervious part of the pixel ( $T_s$ ) is calculated based on canyon temperature ( $T_c$ ) and roof surface  
69 temperature ( $T_r$ ):

$$70 \quad T_s = f_r \times T_r + (1 - f_r) \times T_c \quad \text{Eq. (12)}$$

71 where  $f_r$  is the roof fraction of the impervious surface. Note that the  $T_c$  calculated by the UCM is an  
72 equivalent aerodynamic surface temperature aggregated for canyon surfaces, including walls and roads.  
73 Next, the LST for the whole grid cell is computed as a weighted average based on the  $T_s$  and surface  
74 temperature of pervious part ( $T_1$ ):

$$75 \quad LST = f_{urb} \times T_s + (1 - f_{urb}) \times T_1 \quad \text{Eq. (13)}$$

76 where  $f_{urb}$  is the urban fraction of the pixel."

77 The following is **REMOVED** from the manuscript (abstract):

78 "However, the model still underestimates remotely sensed LST values over highly developed areas. We  
79 hypothesize that the LST underestimation is due to structural formulation in the UCM and cannot be  
80 immediately solved with available parameter choices."

81 The followings are **REMOVED** from the manuscript (section 7.2):

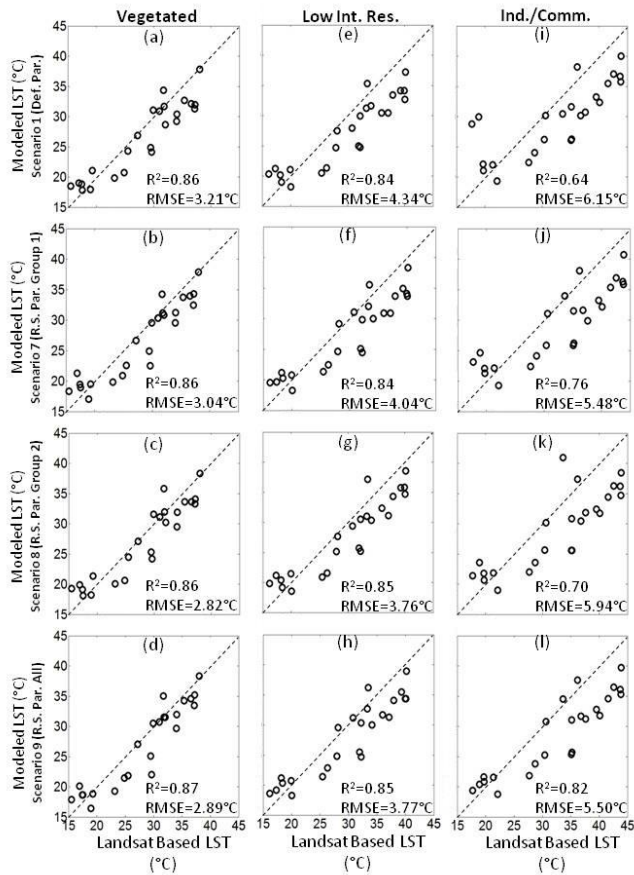
82 "Further analysis (not shown here) indicates that underestimation of LST values is due to a fundamental  
83 problem in the UCM and cannot be immediately solved with available parameter choices. This problem is  
84 discussed in a related study investigating different schemes for LST and conductive heat fluxes in the  
85 UCM [Wang et al. 2011b]. Their study shows that the current UCM formulation results in a phase lag and  
86 cold biases in simulated surface temperature when compared to observations. The discussed cold biased  
87 could potentially be resolved utilizing a spatially-analytical scheme introduced by Wang et al. [2011b]."

88 "Regardless of the parameterization processes, cold biases are persistent in all simulations, particularly  
89 over high intensity residential and industrial/commercial pixels (Fig. 6). As explained above, this  
90 underestimation of LST values is consistent with the literature and is reported to be due to a fundamental  
91 problem in the UCM which produces a phase lag and cold biases in simulated LST [Wang et al., 2011b]."

92 The following is **REMOVED** from the manuscript (section 8):

93 "Nevertheless, the model still underestimates remotely sensed LST values, over highly developed areas.  
94 We speculate that the underestimation of LST values, particularly over high intensity residential and  
95 industrial/commercial areas, is due to structural parameterization in the UCM and cannot be  
96 immediately solved with available parameter choices."

97 The following figure is **REMOVED** from the manuscript:

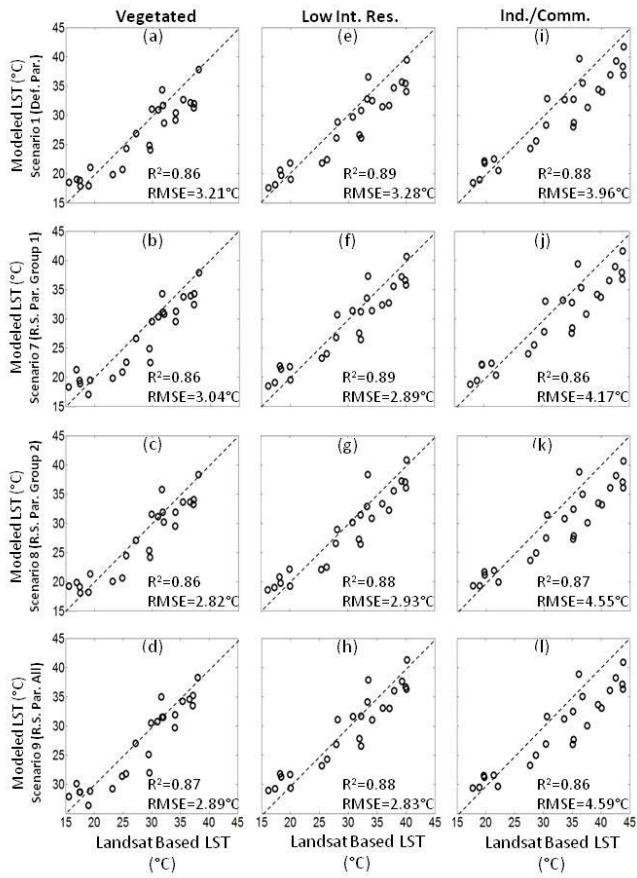


98

99 **Figure 5. Scatter plots of observed (Landsat-based) versus simulated LSTs averaged over different land cover**  
 100 **types using different urban surface parameterizations, including scenarios 1 (first row), 7 (second row)**  
 101 **8 (third row), and 9 (forth row) in Table 1.**

102

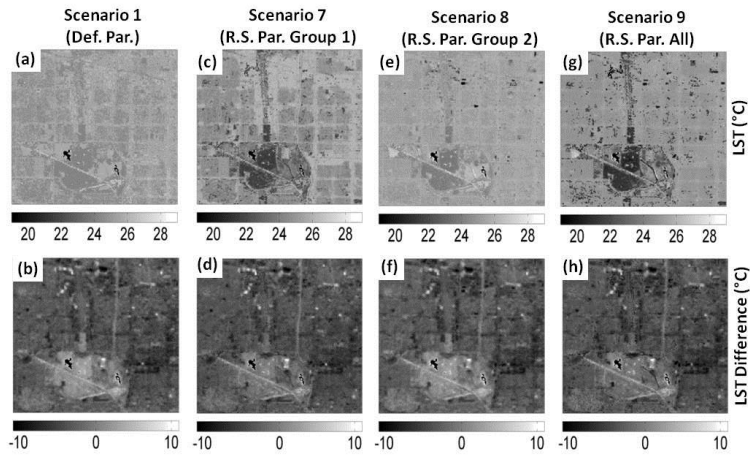
103 The following figure is **ADDED** to the manuscript:



104  
 105 **Figure 5. Scatter plots of observed (Landsat-based) versus simulated LSTs averaged over different land cover**  
 106 **types using different urban surface parameterizations, including scenarios 1 (first row), 7 (second row), 8 (third**  
 107 **row), and 9 (fourth row) in Table 1.**

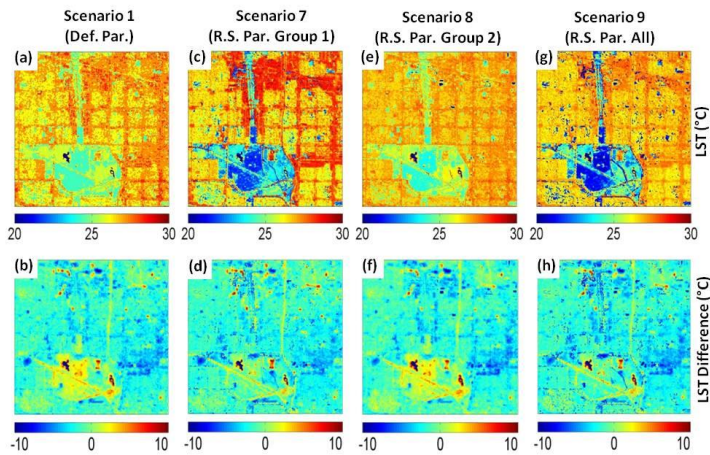
108  
 109  
 110  
 111  
 112  
 113

114 The following figure is **REMOVED** from the manuscript:



115  
116 **Figure 6. Noah/UCM simulated LST maps using different urban surface parameterizations: scenarios 1, 7, 8, and**  
117 **9 from Table 1 (top row) as well as differences between simulated and observed land surface temperature at**  
118 **1100 LST on 14 April 2011 (bottom row).**

119 The following figure is **ADDED** to the manuscript:



120  
121 **Figure 6. Noah/UCM simulated LST maps using different urban surface parameterizations: scenarios 1, 7, 8, and**  
122 **9 from Table 1 (top row) as well as differences between simulated and observed land surface temperature at**  
123 **1100 LST on 14 April 2011 (bottom row).**

124

125 References:

126 Li, D., E. Bou-Zeid, 2014: Quality and Sensitivity of High-Resolution Numerical Simulation of Urban Heat  
127 Islands. Environmental Research Letters, 9, 055001 doi:10.1088/1748-9326/9/5/055001

128

129 **Discussion/Conclusions: It would be useful if the authors could provide some comment on how their**  
130 **choice of urban canopy model affects their results. The Noah-UCM is widely used in offline and**  
131 **coupled simulations, so it makes perfect sense to focus on it. But given the challenge of ascribing**  
132 **physical meaning to parameters in a singlelayer urban canopy model it would be interesting to include**  
133 **some reflection on how the RS parameterization problem would map onto multilayer urban canopy**  
134 **models like the Building Effect Parameterization (BEP), which is now a standard option in WRF. My**  
135 **understanding is that single layer urban canopy models still outperform multilayer models in many**  
136 **applications, but given the greater realism of multilayer representations one might think that**  
137 **improved parameterization methods (such as those described in this paper) could also be usefully**  
138 **applied to multilayer models.**

139 We agree with the reviewer's comment and **added** the following to the manuscript (section 8:  
140 Conclusions):

141 *" Although this study focuses on the widely used single layer UCM, we speculate that implementation of*  
142 *the more accurate remote sensing based parameters (particularly, GVF and ISA) may also enhance*  
143 *performance of the Noah-BEP [Martilli et al., 2002], which is currently the most sophisticated urban*  
144 *scheme in WRF. In this multi-layer UCM a similar approach to the single layer UCM is used based on an*  
145 *urban fraction (or ISA) parameter that couples the Noah outputs over pervious portion of pixels and UCM*  
146 *outputs over developed surfaces."*

147

148 **High Resolution Land Surface Modeling Utilizing Remote Sensing Parameters and the Noah-**

149 **UCM: A Case Study in the Los Angeles Basin**

150

151 **P. Vahmani<sup>1</sup> and T.S. Hogue<sup>2,1</sup>**

152 <sup>1</sup>University of California, Los Angeles, CA

153 <sup>2</sup>Colorado School of Mines, Golden, CO

154

155 Re-submission to HESS

**Deleted:** Submitted

156 October 2014

**Deleted:** April

157

158 *Corresponding Author:*  
159 Terri S. Hogue  
160 Civil and Environmental Engineering  
161 Colorado School of Mines  
162 1500 Illinois Street  
163 Golden, CO 80401  
164 [thogue@mines.edu](mailto:thogue@mines.edu)  
165 303-384-2588  
166



169 **ABSTRACT**

170 In the current work we investigate the utility of remote sensing based surface parameters in the Noah-  
171 UCM (urban canopy model) over a highly developed urban area. Landsat and fused Landsat-MODIS data  
172 are utilized to generate high resolution (30 m) monthly spatial maps of green vegetation fraction (GVF),  
173 impervious surface area (ISA), albedo, leaf area index (LAI), and emissivity in the Los Angeles  
174 metropolitan area. The gridded remotely sensed parameter datasets are directly substituted for the  
175 land-use/lookup-table-based values in the Noah-UCM modeling framework. Model performance in  
176 reproducing ET (evapotranspiration) and LST (land surface temperature) fields is evaluated utilizing  
177 Landsat-based LST and ET estimates from CIMIS (California Irrigation Management Information System)  
178 stations as well as in-situ measurements. Our assessment shows that the large deviations between the  
179 spatial distributions and seasonal fluctuations of the default and measured parameter sets lead to  
180 significant errors in the model predictions of monthly ET fields (RMSE= 22.06 mm/month). Results  
181 indicate that implemented satellite derived parameter maps, particularly GVF, enhance the Noah-UCM  
182 capability to reproduce observed ET patterns over vegetated areas in the urban domains (RMSE= 11.77  
183 mm/month). GVF plays the most significant role in reproducing the observed ET fields, likely due to the  
184 interaction with other parameters in the model. Our analysis also shows that remotely sensed GVF and  
185 ISA improve the model capability to predict the LST differences between fully vegetated pixels and  
186 highly developed areas.

187 **Key words: Noah LSM, UCM, remote sensing, urban hydrology, evapotranspiration, Los Angeles**

**Deleted:** However, the model still underestimates remotely sensed LST values over highly developed areas. We hypothesize that the LST underestimation is due to structural formulation in the UCM and cannot be immediately solved with available parameter choices.

193 **1. Introduction**

194 Urbanization introduces significant changes to land surface characteristics that ultimately perturb land-  
195 atmosphere fluxes of sensible heat, latent heat, and momentum which, in turn, alter atmospheric  
196 properties as well as local weather and climate [Landsberg, 1981; Kalnay and Cai, 2003; Miao et al.,  
197 2009; Ridder et al., 2012]. Urban surfaces are covered with variety of materials with distinct thermal,  
198 radiative, and moisture properties influencing surface energy and water budgets [Arnfield, 2003].  
199 Moreover, contrasting aerodynamic properties of buildings significantly change surface roughness  
200 [Cotton & Pielke, 1995]. The effects associated with modified urban landscapes extend to air quality  
201 [Taha et al., 1997], local temperatures [Bornstein, 1987; Van Wevenberg et al., 2008], local and regional  
202 atmospheric circulation [Pielke et al., 2002; Marshall et al., 2004; Niyogi et al., 2006], and regional  
203 precipitation patterns [Changnon and Huff, 1986; Changnon, 1992; Lowry, 1998].

204 Mesoscale meteorological models have been increasingly applied over urban areas to examine  
205 the urban-atmosphere exchange of heat, moisture, momentum or pollutants. Recently updated  
206 parameterization in the community Weather Research and Forecasting (WRF) model includes coupling  
207 between the Noah LSM (Land Surface Model) and a single layer urban canopy model (UCM) [Kusaka et  
208 al. 2001; Kusaka and Kimura, 2004] which has substantially advanced the understanding and modeling  
209 of the mesoscale impact of cities. The coupled WRF-Noah-UCM has been applied to major metropolitan  
210 regions around the world (e.g. Houston, Beijing, Guangzhou/Hong Kong, , Salt Lake City, and Athens) to  
211 better understand the contribution of urbanization to changes in urban heat island, surface ozone,  
212 horizontal convective rolls, boundary layer structure, contaminant transport and dispersion, and heat  
213 wave events [Chen et al., 2004; Jiang et al., 2008; Miao and Chen, 2008; Miao et al., 2009; Wang et al.,  
214 2009; Tewari et al., 2010; Wei-guang et al., 2011; Giannaros et al., 2013]. A common concern with the  
215 use of these complex mesoscale models, however, is the high level of uncertainty in the specification of  
216 surface cover and geometric parameters [Loridan et al., 2010; Chen et al., 2011]. Although realistic

217 representation of surface properties is critical for accurate simulation of the physical processes  
218 occurring in urban regions, the majority of previous modeling studies rely on traditional land-use data  
219 and lookup tables to define surface parameters.

220 Remote sensed observations provide important spatial information on urban-induced physical  
221 modifications to the Earth's surface [Jin and Shepherd, 2005]. Airborne LIDAR (Light Detection and  
222 Ranging) systems and photogrammetric techniques have been utilized to produce morphological  
223 parameters over urban areas [Burian et al., 2004, 2006, 2007; Taha, 2008; Ching et al., 2009]. Burian et  
224 al. [2004] used airborne LIDAR data, at 1 m resolution, to generate datasets of 20 urban canopy  
225 parameters (e.g., building height, height-to-width ratio, and roughness length) for an air quality  
226 modeling study over Houston, Texas. Taha [2008] introduced an alternative and low-cost approach for  
227 generating urban canopy parameters input for the uMM5 over Sacramento region, California. The study  
228 relied on commercially available Google Earth PRO imagery to generate urban geometry parameters  
229 (e.g., pavement land-cover fraction, roof cover fraction, and mean building height). Using LIDAR-based  
230 three-dimensional data sets of buildings and vegetation, Ching et al. [2009] presented a high-resolution  
231 database of the geometry, density, material, and roughness properties of the morphological features for  
232 applications in WRF and other models over Houston, Texas. While promising, the availability of such  
233 datasets is currently limited to a few geographical locations and the reproduction of such datasets is  
234 extremely challenging due to high collection costs and data management difficulties associated with the  
235 extremely large size of LIDAR datasets [Burian et al., 2006; Ching et al., 2009].

236 Observations from satellites, on the other hand, have been utilized in model validation  
237 processes over urban areas [Miao et al., 2009; Giannaros et al., 2013]. In addition to in situ observations,  
238 Giannaros et al. [2013] included MODIS (Moderate Resolution Imaging Spectroradiometer) based Land  
239 Surface Temperature (LST) products in their modeling study of the urban heat island (UHI) over Athens,  
240 Greece. Similarly, Miao et al. [2009] utilized 1-km-resolution MODIS data to verify the WRF-Noah-UCM

Deleted: Taha

242 simulated LST distribution in Beijing. Other studies have employed satellite data to replace outdated  
243 urban land use maps in atmospheric models with new remote sensing products [Cheng and Byun, 2008;  
244 Cheng et al., 2013]. Focusing on boundary layer mixing conditions and local wind patterns in the  
245 Houston Ship channel, Cheng and Byun [2008] reported that the Noah LSM and planetary boundary  
246 layer (PBL) scheme performances in the MM5 were improved when land-use type distributions were  
247 correctly represented in the model using high resolution Landsat-based land use data. Cheng et al.  
248 [2013] compared WRF simulations in the Taiwan area using U.S. Geological Survey (USGS), MODIS, and  
249 SPOT (Système Pour l'Observation de la Terre) based land use data. Using the new high resolution land  
250 use types obtained from SPOT satellite imagery, the WRF predictions of daytime temperatures and  
251 onshore sea breezes had the best agreement with observed data. Furthermore, more accurate surface  
252 wind speeds were simulated when MODIS and SPOT data replaced conventional USGS land use maps in  
253 the WRF runs due to the more realistic representation of roughness length in the remotely sensed  
254 databases. Although these and other previous studies [e.g., Jin and Shepherd, 2005] have recognized the  
255 usefulness of satellite imagery (e.g., NASA's Terra, Aqua, and Landsat data) in specifying surface physical  
256 characteristics in urban environments, very few have directly incorporated high resolution gridded  
257 satellite-based parameters (e.g., impervious surface area, albedo, and emissivity) into parameter  
258 estimation within land surface/atmospheric modeling systems.

259 In the current work we investigate the utility of remote sensing based surface parameters in the  
260 Noah-UCM modeling framework over a highly developed urban area. Among parameters that can be  
261 related to a measurable physical quantity, we evaluate those routinely and freely obtained from  
262 satellite-based platforms. The derived parameter sets are implemented in the Noah-UCM with a focus  
263 on simulated surface energy and water cycles that are essential feedback to the widely used WRF  
264 model. Landsat and fused Landsat-MODIS data are utilized to generate high resolution (30 m) monthly  
265 spatial maps of green vegetation fraction (GVF), impervious surface area (ISA), albedo, leaf area index

Deleted: later

267 (LAI), and emissivity in the Los Angeles metropolitan area. The temporal and spatial distributions of  
268 newly assigned parameters are compared with those based on the model lookup tables. Next, gridded  
269 remotely sensed parameter datasets are directly incorporated into the Noah-UCM modeling framework  
270 replacing the land-use/lookup-table-based values. The sensitivity of the simulated energy and water  
271 fluxes to the newly developed spatial metrics of parameters is presented. The model's performance in  
272 reproducing evapotranspiration (ET) and LST fields is evaluated utilizing Landsat-based land surface  
273 temperature and ET estimates from CIMIS (California Irrigation Management Information System)  
274 stations as well as in-situ measurements. Finally, the influence of each parameter set on the urban  
275 energy and water budgets is investigated.

276

## 277 **2. Study Area**

278 The study domain is a 49 km<sup>2</sup> highly developed neighborhood in the City of Los Angeles (Fig. 1). Los  
279 Angeles is the second most populous city in the United States with a population of 3.8 million [U.S.  
280 Census, 2011], covering an area of 1,215 km<sup>2</sup> in Southern California. The City has a Mediterranean  
281 climate and receives 381 mm of annual precipitation, mostly over the winter months [NOAA-CSC, 2003;  
282 SCDWR, 2009]. Due to the semi-arid nature of the region, the City's water supply is heavily dependent  
283 on imported water (52% from the Colorado River and 36% from the Los Angeles Aqueduct) [LADWP,  
284 2010]. Regional water demands and the extensive dependence on external sources make accurate  
285 spatial representation of the metropolitan area in regional land surface/atmospheric models imperative  
286 for predicting current and future water budgets. The study domain includes commercial/industrial as  
287 well as low and high intensity residential land cover types and a large park with both irrigated and non-  
288 irrigated landscapes (Fig. 1b and 1c).

289

290

291 **3. Remotely Sensed Parameters**

292 Remote sensing data are retrieved from Landsat ETM+ images with a nominal pixel resolution of 30 m in  
293 the short wave bands and 60 m in the thermal band. The level 1Gt ETM+ imagery from USGS EROS,  
294 spanning years 2010-2011, are calibrated and atmospherically corrected through the Landsat Ecosystem  
295 Disturbance Adaptive Processing System (LEDAPS). Study domain data are not affected by the failure of  
296 the Landsat-7 ETM+ Scan Line Corrector in 2003 (SLC-off). Employing a knowledge-based approach,  
297 similar to the one introduced by Song and Civco [2002], several binary masks are applied to the images  
298 to detect contaminated areas (cloud and shadow). Images with cloud and/or shadow are distinguished  
299 and omitted in the following parameter retrievals. A total of 24 pure images, acquired over two years,  
300 are utilized in the parameter estimation processes.

Deleted: 2033

301 In addition to Landsat observations, MODIS products from Terra and Aqua satellite platforms  
302 are also utilized. The MODIS MCD43A BRDF (Bidirectional Reflectance Distribution Function) products,  
303 concurrent with pure Landsat images, are collected for use in the parameter calculations. The 500-m  
304 BRDF products are generated by the MODIS Adaptive Processing System (MODAPS) at the Goddard  
305 Space Flight Center (GSFC), using a kernel-driven linear model, and distributed through the Land  
306 Processes DAAC (Distributed Active Archive Center) [Justice et al., 2002; Schaaf et al., 2002; Shuai et al.,  
307 2008]. The described Landsat and MODIS-based data are used to produce a group of six remotely sensed  
308 derivatives:

- 309 • *Green Vegetation Fraction (GVF)*: GVF spatial maps are derived according to Gutman and  
310 Ignatov [1998] utilizing NDVI (Normalized Difference Vegetation Index) measurements. First,  
311 atmospheric corrected reflectance values from the red ( $\rho_{ETM3}$ ) and near-infrared ( $\rho_{ETM4}$ ) bands of Landsat  
312 ETM+ are used to derive NDVI maps for each date of imagery based on Eq. 1. Next, assuming the  
313 vegetated part of a pixel is covered by dense vegetations (i.e., it has a high LAI), GVF is calculated using  
314 Eq. 2.

316 
$$NDVI = \frac{\rho_{ETM4} - \rho_{ETM3}}{\rho_{ETM4} + \rho_{ETM3}} \quad \text{Eq. (1)}$$

317 
$$GVF = \frac{NDVI - NDVI_0}{NDVI_{\infty} - NDVI_0} \quad \text{Eq. (2)}$$

318 Where  $NDVI_0$  and  $NDVI_{\infty}$  are constant values computed using signals from bare soil and densely  
319 vegetated pixels in the study domain, respectively.

320 • *Impervious Surface Area (ISA)*: ISA is shown to be inversely proportional to vegetation fraction  
321 where non-vegetated pervious surfaces are rare [Bauer et al., 2007]. Since the majority of pervious  
322 surfaces in the studied domain are vegetated and heavily irrigated throughout the year, ISA is assumed  
323 to be the complement of the vegetation fraction:

324 
$$ISA = (1 - GVF_{max}) \cdot 100 \quad \text{Eq. (3)}$$

325 Where  $GVF_{max}$  is the maximum GVF detected over the two year study period. The produced ISA map  
326 shows high accuracy (>95%) when compared to a previously developed high resolution land cover map,  
327 based on QuickBird remote sensing data, aerial photographs, and geographic information systems over  
328 the city of Los Angeles [McPherson et al., 2008]. We speculate that one cause contributing to the high  
329 accuracy of this assumption is that ISA overestimation, induced by non-vegetated pervious surfaces, is  
330 offset by tree canopies that cover areas larger than underlying pervious surfaces.

Deleted: that may contribute

331 • *Albedo*: Employing a recent methodology by Shuai et al. [2011], 30 m land surface albedo maps  
332 is generated utilizing Landsat surface reflectance and anisotropy information from concurrent 500 m  
333 MODIS BRDF products. Landsat data are reprojected from UTM to MODIS sinusoidal projection and  
334 aggregated from 30 m to 500 m. Using USGS-based land cover types, the percentage of each land cover  
335 class within each MODIS pixel is computed, then relatively pure pixels (>85% purity) are selected for  
336 each class. MCD43A2 quality assessment product is used to choose highest quality MODIS MCD43A1

338 BRDF parameters for the pure pixels. The concurrent parameters are used to calculate nadir  
 339 reflectance, white sky albedo, and black sky albedo under the solar geometry at Landsat overpass time  
 340 and MODIS scale. Next, the spectral albedo-to-nadir reflectance ratios, for white sky and black sky  
 341 albedos, are calculated over the pure pixels. The resultant ratios, specific to each land cover class, are  
 342 applied to Landsat surface reflectance to generate the spectral white sky and black sky albedos for each  
 343 Landsat pixel. A further narrowband-to-broadband conversion based on extensive radiative transfer  
 344 simulations by Liang [2000] is applied to generate the broadband albedos at shortwave regime. Finally,  
 345 albedo (blue sky) is modeled as an interpolation between the black sky ( $\alpha_{bs}$ ) and white sky ( $\alpha_{ws}$ ) albedos  
 346 as a function of the fraction of diffuse skylight ( $S(\theta, \tau(\lambda))$ ) which is estimated by the 6S (Second Simulation  
 347 of the Satellite Signal in the Solar Spectrum) codebase (Eq. 4) [Schaaf et al., 2002].

$$348 \quad \alpha(\theta, \lambda) = \{1 - S(\theta, \tau(\lambda))\} \alpha_{bs}(\theta, \lambda) + S(\theta, \tau(\lambda)) \alpha_{ws}(\theta, \lambda) \quad \text{Eq. (4)}$$

349 where  $\tau$ ,  $\theta$ , and  $\lambda$  are optical depth, solar zenith, and wavelength, respectively.

- 350 • *Leaf Area Index (LAI)*: Stenberg et al. [2004] showed that a reduced simple ratio (RSR) explains  
 351 63%-75% of the variations in LAI and that maps of projected LAI, based on RSR, have good agreement  
 352 with observations. In the current study, LAI values are retrieved based on the LAI-RSR correlations which  
 353 are specified utilizing table-based LAI estimates in pure (fully vegetated) pixels and remotely sensed RSR  
 354 maps. The atmospheric corrected reflectance values of Landsat ETM spectral channels red ( $\rho_{ETM3}$ ), near  
 355 infrared ( $\rho_{ETM4}$ ), and mid infrared ( $\rho_{ETM5}$ ), implemented in the following equation (Eq. 5), define RSR:

$$356 \quad RSR = \frac{\rho_{ETM4}}{\rho_{ETM3}} \cdot \frac{\rho_{5max} - \rho_{ETM5}}{\rho_{5max} + \rho_{5min}} \quad \text{Eq. (5)}$$

357 where  $\rho_{ETM5min}$  and  $\rho_{ETM5max}$  are the smallest and largest mid infrared reflectance detected in the Landsat  
 358 ETM images over the study domain, excluding open water pixels.



359 • *Emissivity*: Among various methods developed to define land surface emissivity, the NDVI  
 360 Thresholds Method (NDVI<sup>THM</sup>) has been widely applied to urban areas [Stathopoulou and Cartalis, 2007;  
 361 Stathopoulou et al., 2007; Tan and Li, 2013]. NDVI<sup>THM</sup> is superior to other methods since the  
 362 consideration of the internal reflections (cavity effects), caused by heterogeneous surfaces minimizes  
 363 the overall error in this approach [Sobrino et al., 2001]. This methodology, originally introduced by  
 364 Sobrino and Raissouni [2000] and modified later by Stathopoulou et al. [2007] for urban areas, is  
 365 selected for land surface emissivity estimation in the current work. Using the Landsat-based NDVI  
 366 thresholds, the study area is divided into four classes: (1) fully vegetated (NDVI>0.5), (2) built-up areas  
 367 with sparse vegetation (NDVI≤0.2), (3) mixture of man-made material and vegetation (NDVI>0.2 and  
 368 ≤0.5), and (4) water bodies (NDVI<0). Mean emissivity values of 0.980, 0.920, and 0.995 are then used  
 369 for fully vegetated, built-up and water pixels [Similar to Tan and Li, 2013]. Emissivity values (ε) for mixed  
 370 pixels (class 3) are estimated using the following equations [for details see Stathopoulou et al., 2007]:

$$371 \quad \varepsilon = 0.017P_V + 0.963 \quad \text{Eq. (6)}$$

$$372 \quad P_V = \frac{(NDVI-0.2)^2}{(0.5-0.2)^2} \quad \text{Eq. (7)}$$

373 • *Land Surface Temperature (LST)*: The emissivity corrected land surface temperature (LST) is  
 374 calculated as follows [Artis & Carnahan, 1982]:

$$375 \quad LST = \frac{BT}{\left\{1 + \left[\frac{\lambda BT}{\rho} \cdot \ln \varepsilon\right]\right\}} \quad \text{Eq. (8)}$$

376 where BT is Landsat at sensor brightness temperature (K); λ and ε are the wavelength of emitted  
 377 radiance (11.5 μm) and surface emissivity; ρ = hc/σ (1.438 × 10<sup>-2</sup> m K); σ, h, and c are Boltzmann  
 378 constant, Planck's constant, and the velocity of light, respectively.

379

## 380 4. Numerical Modeling System

### 381 4.1. Noah LSM-UCM Model

382 Land surface processes are parameterized using the offline Noah LSM [Chen and Dudhia, 2001] coupled  
383 with the single layer UCM [Kusaka et al. 2001; Kusaka and Kimura, 2004]. The Noah LSM is based on a  
384 diurnally dependant Penman potential evaporation approach, a multi-layer soil parameterization, a  
385 canopy resistance model, surface hydrology, and frozen ground physics [Chen et al., 1996, 1997; Chen  
386 and Dudhia, 2001; Ek et al., 2003]. The UCM parameterization includes urban building geometry,  
387 shadowing from buildings, reflections and trapping of radiation in a street canyon, and an exponential  
388 wind profile. The Noah LSM provides surface sensible and latent heat fluxes and surface skin  
389 temperature for vegetated areas (e.g., parks and trees) and the UCM calculates the fluxes for  
390 impervious surfaces. The outputs from the Noah LSM and UCM are coupled through the urban surface  
391 fractions.

### 392 4.2. Irrigation Module

393 Irrigation is accounted for, in the Noah-UCM modeling framework, by incorporating an urban irrigation  
394 module developed in our previous work [Vahmani and Hogue, 2013; 2014]. The developed irrigation  
395 scheme mimics the effects of urban irrigation by increasing soil moisture content in vegetated portion of  
396 grid pixels at a selected interval. Added anthropogenic soil moisture contribution is a function of the soil  
397 moisture deficit, which is the difference between irrigated soil moisture content and actual soil moisture  
398 content in the top soil layer. The irrigation module calculates irrigated soil moisture content ( $SMC_{IRR}$ ;  $m^3$   
399  $m^{-3}$ ), soil moisture deficit (DEF;  $m^3 m^{-3}$ ), and irrigation water (IRR;  $kg m^{-2} s^{-1}$ ) as:

$$400 \quad SMC_{IRR} = \alpha \cdot SMC_{max} \quad \text{Eq. (9)}$$

$$401 \quad DEF = \max\{[SMC_{IRR} - SMC_1], 0\} \quad \text{Eq. (10)}$$

$$402 \quad IRR = \frac{\rho_w}{\Delta t} DEF \cdot D_1 \quad \text{Eq. (11)}$$

403 where saturation soil moisture content ( $SMC_{max}$ ;  $m^3 m^{-3}$ ) and irrigation demand factor ( $\alpha$ ; unit less)  
404 define irrigated soil moisture content (Eq. 9);  $D_1$  is top soil layer thickness (10 cm);  $\rho_w$  ( $kg m^{-3}$ ) and  $\Delta t$   
405 stand for water density and Noah-UCM time step (3600 s), respectively. The parameter  $\alpha$ , ranging from  
406 zero to one, regulates the amount of irrigation water added to the soil each time the scheme increases  
407 the soil moisture, simulating an irrigation event. Similar to previous studies [Hanasaki et al. 2008a,  
408 2008b; Pokhrel et al. 2012] an irrigation demand factor of 0.75 is utilized in the current work. The  
409 irrigation interval is set to three times per week according to the water restrictions implemented by Los  
410 Angeles Department of Water and Power (LADWP) in 2010 (LADWP, personal communication, 2013).

#### 411 4.3. Improving the UCM-simulated LST

Deleted: 4.3.

412 The calculation of the impervious surface temperature in the UCM version used in this study has been  
413 shown to be inaccurate [Li and Bou-Zeid, 2014]. This is due to the fact that the turbulent transfer  
414 coefficient ( $C_h$ ) for the whole pixel is calculated using only momentum and thermal roughness lengths of  
415 vegetated portion, ignoring the developed surface impact on  $C_h$ . Li and Bou-Zeid [2014] showed that this  
416 inconsistency could result in large biases in simulated LST values. In the current study, an alternative LST  
417 calculation, proposed by Li and Bou-Zeid [2014], is used as follows. First, a revised surface temperature  
418 of the impervious part of the pixel ( $T_s$ ) is calculated based on canyon temperature ( $T_c$ ) and roof surface  
419 temperature ( $T_r$ ):

$$420 T_s = f_r \times T_r + (1 - f_r) \times T_c \text{----- Eq. (12)}$$

421 where  $f_r$  is the roof fraction of the impervious surface. Note that the  $T_c$  calculated by the UCM is an  
422 equivalent aerodynamic surface temperature aggregated for canyon surfaces, including walls and roads.  
423 Next, the LST for the whole grid cell is computed as a weighted average based on the  $T_s$  and surface  
424 temperature of pervious part ( $T_1$ ):

$$425 LST = f_{urb} \times T_s + (1 - f_{urb}) \times T_1 \text{----- Eq. (13)}$$

426 where  $f_{urb}$  is the urban fraction of the pixel.

428 **4.4. Land Cover Data and Forcing Fields**

429 The Noah-UCM modeling system requires static data to describe physical characteristics of the surface,  
430 including soil type, slope type, vegetation type, and urban type. A combination of the Soil Data Mart  
431 [<http://soildatamart.nrcs.usda.gov>] and the Los Angeles Department of Public Works (LADPW)  
432 databases are used to gather soil classification information. Land use and land cover are parameterized  
433 using the 30 m NOAA C-CAP-2006 land cover data which is transformed to urban and vegetation type  
434 spatial maps over the study domain. High, medium, and low intensity developed land cover types,  
435 recognized by NOAA, are converted to UCM Industrial/Commercial, high and low intensity residential  
436 types, respectively. The developed open space along with natural land types are categorized as one of  
437 the 27 Noah LSM vegetation classes.

438 The offline Noah LSM-UCM is forced utilizing hourly ground-based observations from CIMIS and  
439 National Climatic Data Center (NCDC) stations for the period from 1 January 2010 to 31 December 2011.  
440 There are ten CIMIS and eight NCDC stations within close proximity of the study domain (Figure 1a). The  
441 NCDC stations, which use Automated Surface Observing Systems (ASOS), are located at smaller local  
442 airports (6 stations), one major airport (Los Angeles International Airport), and a university campus  
443 (University of Southern California; USC) within the Los Angeles metropolitan area. Reporting the  
444 meteorological conditions, the NCDC stations are used for wind speed, air temperature, relative  
445 humidity, air pressure, and incoming long wave radiation. All NCDC data are gathered at a standard  
446 reference height of 2m. The regional CIMIS stations are utilized for solar radiation (using LI2005  
447 pyranometer) and tipping bucket rain gauges in 18 stations (NCDC and CIMIS) are included in collection  
448 of precipitation data. Inverse-distance weighting (2<sup>nd</sup> power) is employed to create the spatial gridded  
449 forcing fields. Linear interpolation and data from the nearest gage are utilized to replace missing data.

450

451 **5. Numerical Experiments and Evaluation Methods**

452 **5.1. Remote Sensing Based Parameterization**

453 To investigate the sensitivity of the Noah-UCM model to integration of the developed remotely sensed  
454 parameters, nine simulation scenarios are designed (Table 1). A control experiment (Scenario 1) is  
455 conducted in which all default parameters are utilized in the Noah-UCM. Scenarios 2 to 6 explicitly  
456 assess each individual parameter effects on urban energy and water budgets using the newly  
457 incorporated remote sensing parameters. Scenario 7 analyzes the effects of employing both remotely  
458 sensed GVF and ISA while Scenario 8 assesses simultaneous integration of albedo, LAI, and emissivity.  
459 We are interested in the comparison of Scenarios 7 and 8 as the Noah-UCM parameterizations use GVF  
460 and ISA to select albedo, LAI, emissivity, and roughness length values from the predefined ranges in the  
461 parameter tables. It is worth mentioning that GVF alters the roughness length values over pervious or  
462 natural areas. However, roughness length and building height over the impervious surfaces are kept at  
463 the default values listed by Chen et al. [2011]. Scenarios 7 and 8 help quantify the contribution of each  
464 parameter group to the model's ability to reproduce the observed surface states and fluxes. Finally, the  
465 last experiment (Scenario 9) implements all five remotely sensed parameter sets in the simulations. It  
466 should be noted that the GVF and LAI measurements over mixed pixels (vegetated urban areas) are  
467 scaled up by multiplying the remotely sensed values by  $1/(1 - \text{urban fraction})$  since in the Noah-UCM  
468 modeling framework these parameters characterize only the pervious portion (1 - urban fraction) of  
469 each pixel. However, remotely sensed albedo and emissivity values over each pixel are assigned to both  
470 pervious and impervious surfaces for that pixel. Other than the implemented remote sensing based  
471 parameters, the rest of the model parameters are kept at default values. All experiments incorporate  
472 the irrigation module and irrigation rates are kept constant in all scenarios. All scenarios are run at 30 m  
473 spatial and 1 hour temporal resolutions, spanning 2010 and 2011, with the first three months used as  
474 model initialization.

475 **5.2. Model Evaluation Approach**

Deleted: using urban fractions

Deleted: ,

Deleted: ,

Deleted: sending

480 In order to evaluate the performance of the Noah-UCM modeling framework, simulated LSTs are  
481 compared with concurrent Landsat observations and simulated latent heat flux time series are assessed  
482 against CIMIS-based ET observations. The CIMIS network was established in 1982 by the CDWR  
483 (California Department of Water Resources) and the University of California at Davis in order to provide  
484 real-time weather conditions and irrigation water need estimates for California's agricultural  
485 community. The automated CIMIS stations measure hourly surface solar radiation, temperature,  
486 humidity, wind, precipitation, soil temperature, and surface pressure [http://www.cimis.water.ca.gov].  
487 Employing observed meteorological fields over a well-watered soil, the reference ET ( $ET_0$ ) is calculated  
488 for each site. Utilizing a methodology introduced by CDWR [2000], actual urban landscape ET is  
489 estimated using  $ET_0$  and a landscape coefficient, which is a function of species, density, and  
490 microclimate factors. Based on the authors' knowledge in the study landscape as well as a report by  
491 CDWR [2000], we assume "Moderate" (trees and shrubs) and "High" (turf grass) water needs. Following  
492 the CDWR [2002] instructions on irrigation zones with mixed water need categories (i.e., low, moderate,  
493 and high), a value from high category is selected (average species factor=0.80). Assuming the "average"  
494 category for vegetation density, a density factor of 1 is used. Furthermore, a "high" category of  
495 microclimate condition is used (microclimate factor=1.25) for the current highly developed study  
496 domain. This factor is utilized to take into account the contribution of the developed surfaces to the  
497 water loss from vegetated areas, through anthropogenic heating, reflected light, and high temperatures  
498 of surrounding heat-absorbing surfaces (e.g., paving and buildings). Using these factors, a landscape  
499 coefficient of 1 (landscape coefficient = species factor  $\times$  density factor  $\times$  microclimate factor) is  
500 prescribed. This coefficient and  $ET_0$  estimations from ten CIMIS stations within close proximity of the  
501 study domain (Fig. 1a) are utilized to compute the urban landscape ET. Inverse-distance weighting (2<sup>nd</sup>  
502 power) is employed to create spatial gridded ET maps over fully vegetated pixels in the study area which  
503 is then used in validation processes of the Noah-UCM. ET output of the model is also evaluated against

Deleted: /cimis

505 recent ET measurements in the greater Los Angeles area [Moering, 2011]. Moering [2011] employed a  
506 previously developed chamber approach to measure instantaneous ET in an irrigated and a non-  
507 irrigated park in the Los Angeles metropolitan area during WY (Water Year) 2011 (WY is defined as Oct.  
508 1st of the previous year to Sep. 30th of the designated year). They reported an annual ET of about 1224  
509 mm over the observed irrigated park, which is located within our study domain.

510

## 511 **6. Sensitivity Study of Surface Parameters**

### 512 **6.1. Temporal Evaluation**

513 The monthly time series of the default Noah-UCM and remote sensing based GVF, ISA, albedo, and LAI  
514 are compared and modeled cumulative monthly sensible and latent heat fluxes, using default and newly  
515 estimated parameters, are presented over fully vegetated, low intensity residential, and  
516 industrial/commercial areas (Fig. 2). Fluxes from high intensity residential areas are not presented as  
517 they behave similarly to those from the industrial/commercial areas. Except for the summer months,  
518 GVF values are significantly increased throughout the year when remote sensing products are utilized  
519 (Fig. 2a). Moreover, the default seasonal variations of GVF values, assumed over all the land cover types,  
520 are not detected in Landsat imagery (Fig. 2a). The reason for this is the significant and year round  
521 irrigation in the Los Angeles area, which is not accounted for in the default parameter tables. This is  
522 confirmed by previous studies [Johnson and Belitz, 2012] that reported urban vegetation supported by  
523 water delivery, in contrast to common seasonal behavior of greening in the winter/spring and browning  
524 in the summer, maintains constant greenness which is reflected in NDVI and GVF estimates. GVF plays a  
525 dominant role in the Noah-UCM simulations as it defines the vegetated fraction of the natural areas,  
526 and specifies albedo, LAI, emissivity, and roughness length values from the predefined ranges in the  
527 model lookup tables. Furthermore, GVF partitions the total ET between soil direct and canopy ET. The  
528 simulated latent heat flux is considerably decreased (up to 139 MJ m<sup>-2</sup> per month) in the summer time

529 and increased over the remaining months, when remotely sensed GVF is incorporated in the fully  
530 vegetated areas (Fig. 2b). Since any increase of latent heat flux that does not alter the radiative balance  
531 leads to a reduction in sensible flux, the newly developed GVF values, in turn, cause enhancements (up  
532 to 103 MJ m<sup>-2</sup> per month) in the simulated summer sensible heat fluxes and a reduction in the sensible  
533 heat fluxes during the remaining months (Fig. 2b). Latent and sensible heat fluxes from the low intensity  
534 residential pixels show similar but less significant changes (up to 66.1 and 31.0 MJ m<sup>-2</sup> per month,  
535 respectively), when the new parameter sets are implemented. Adding remotely sensed GVF causes  
536 insignificant changes in the industrial/commercial area fluxes due to the small percentage of vegetated  
537 land cover in such areas (Fig. 2d).

538 There are also large deviations between the look-up-table-based ISAs and the remotely sensed  
539 values. Averaged ISA is decreased (10%) over industrial and commercial pixels and increased (49%) over  
540 low intensity residential areas, when remote sensing products are utilized in the parameter estimation  
541 process (Fig. 2.e). These changes in the impervious surface area, or urban fraction values, have  
542 significant effects on monthly latent and sensible heat fluxes over the developed pixels (Fig. 2g and 2h),  
543 due to the critical role of urban fraction in partitioning of the energy fluxes. Over the low intensity  
544 residential areas, higher ISA values minimize the effects of urban vegetation which leads to latent heat  
545 fluxes decreases (up to 62.6 MJ m<sup>-2</sup> per month) and sensible heat fluxes increases (up to 52.4 MJ m<sup>-2</sup> per  
546 month), throughout the year, when remotely sensed data replace default urban fractions (Fig. 2g).  
547 These changes are reversed and less significant over the industrial and commercial pixels (maximum  
548 latent and sensible heat flux changes of 30.0 and 26.5 MJ m<sup>-2</sup> per month, respectively; Fig. 2h). ISA has  
549 no influence on the fluxes from fully vegetated pixels which do not include impervious areas (Fig. 2.f).

550 Considerable changes in the monthly albedo averages are detected when incorporating remote  
551 sensing data in the parameterization process (Fig. 2i). Using fused Landsat and MODIS products, a  
552 reduction of averaged albedo values is observed over the fully vegetated and residential areas (up to

Deleted: MOSID



554 48% and 39%, respectively; Fig. 2i). Moreover, the default seasonal variations are hardly noticeable in  
555 the remote sensing based albedo values, which is due to the consistent greenness in the study area from  
556 irrigation throughout the year. On the other hand, considerable albedo increases (up to 39%) are  
557 detectable over the industrial/commercial pixels (Fig. 2i), which are caused by bright and highly  
558 reflective materials seen mainly over the rooftops of industrial/commercial buildings. Albedo affects the  
559 radiative energy budget and consequently available energy for the turbulent fluxes. In the current study,  
560 decreased albedo values over the fully vegetated and low intensity residential areas result in reduced  
561 loss of solar and long wave radiation respectively and, in turn, increases the sensible heat flux (up to  
562 33.8 and 21.5 MJ m<sup>-2</sup> per month; Fig. 2j and 2k). Albedo induced sensible heat decreases over  
563 industrial/commercial pixels are also noticeable (up to 33.9 MJ m<sup>-2</sup> per month; Fig. 2l).

564 Distinct seasonal fluctuations of LAI are observed in the remotely sensed data and the default parameter  
565 tables (Fig. 2m). This reflects the fact that landscape plantings are quite different from agricultural crops  
566 due to their being composed of collections of vegetation species and affected by complex irrigation  
567 patterns which are not taken into account in the vegetation parameter tables in the Noah LSM [CDWR,  
568 2000; Vahmani and Hogue, 2013; 2014]. Over the heavily vegetated pixels, the default pattern is  
569 reversed in the measured parameter sets with less seasonal variations and peaks in the winter time, due  
570 to the fact that most of the precipitation occurs in the winter months, over the current study domain  
571 (Fig. 2m). The industrial and commercial pixels illustrate higher LAI values in the remotely sensed  
572 parameter maps, year round, when compared to the default values (Fig. 2m). LAI is a critical parameter  
573 in the Noah LSM, which is involved in the parameterization of the canopy resistance, controlling canopy  
574 ET rates. In the presented results (Figs. 2n and 2o), LAI induced changes in the simulated turbulent fluxes  
575 are more apparent in the summer months and over fully vegetated and residential pixels, where  
576 sensible heat flux is significantly increased (up to 57.2 and 86.5 MJ m<sup>-2</sup> per month, respectively) and  
577 latent heat flux is significantly decreased (up to 65.5 and 97.9 MJ m<sup>-2</sup> per month, respectively). This is

578 due to the considerable decreases in the LAI values in summer time which lead to elevations of the  
579 canopy resistance and therefore reductions of the transpiration from the vegetation, causing decreases  
580 in latent heat fluxes. This in turn partitions the net radiation more into sensible heat fluxes. LAI does not  
581 affect fluxes from industrial/commercial pixels with small pervious fractions (Fig. 2p). It is worth  
582 mentioning that changes in the turbulent fluxes time series, in particular the latent heat flux decreases  
583 in the summer months induced by implementation of satellite-based LAI, are to some extent captured in  
584 the simulations with the remote sensing based GVF (compare Fig. 2b with 2n and 2c with 2o). This  
585 reflects our previous point that GVF controls assigned LAI values to vegetated pixels in the Noah LSM  
586 and that realistic presentation of GVF in the modeling framework can enhance LAI inputs in the model  
587 when LAI measurements are not available.

588 Remotely sensed emissivity maps are also utilized to replace the default values in the Noah-  
589 UCM simulations, which results in changes in the emissivity values (up to 5.1%). However, the new  
590 surface parameterization leads to insignificant changes in turbulent fluxes (results now shown). The  
591 largest emissivity induced alterations in sensible heat fluxes are seen over industrial and commercial  
592 pixels (up to 31.2 MJ m<sup>-2</sup> per month). Latent heat fluxes are changed, the most significantly, over fully  
593 vegetated areas (up to 2.56 MJ m<sup>-2</sup> per month).

## 594 **6.2. Spatial Evaluation**

595 The spatial distributions of newly assigned GVF, ISA, albedo, and LAI are next compared with those  
596 based on the Noah-UCM lookup tables. Different urban surface parameterizations, along with their  
597 impacts on the simulated maps of turbulent sensible and latent heat fluxes, are presented (Fig. 3; Valid  
598 at 1100 LST on 14 April 2011). As expected, during the spring period (April), GVF values are significantly  
599 higher when remote sensing products are utilized, due to the irrigation effects which are ignored in the  
600 default parameters (Fig. 3a and 3b). Over fully vegetated and low intensity residential pixels, where a  
601 significant portion of the energy goes into evaporation and transpiration, latent heat flux increases

602 (about 300 and 230 W m<sup>-2</sup>, respectively) and sensible heat fluxes decreases (about 160 and 120 W m<sup>-2</sup>,  
603 respectively) are found (Fig. 3c and 3d) when utilizing the remote sensing GVF.

604 The spatial distributions of ISA, or urban fraction, between the remote sensing and default values show  
605 similar patterns (Fig. 3e and 3f). However, industrial/commercial and high intensity residential areas are  
606 assigned noticeably higher urban fraction values in the remote sensing based maps (compare Fig. 3e and  
607 3f) which leads to lower latent heat fluxes (bias of up to about 130 W m<sup>-2</sup>) and higher sensible (bias of up  
608 to about 100 W m<sup>-2</sup>) in these pixels (Fig. 3g and 3h).

609 The Noah-UCM parameters, based on look-up tables, underestimate surface albedo values over  
610 highly urbanized pixels, when compared with remote sensing data (Fig. 3i and 3j). In particular, the  
611 industrial/commercial buildings with highly reflective rooftops are completely ignored. Over the highly  
612 vegetated areas, however, albedo values are slightly overestimated in look-up tables. Altering the  
613 energy budget, the newly developed albedo datasets lead to lower Noah-UCM-simulated sensible heat  
614 fluxes over intensely developed pixels (Fig. 3k). The sensible heat flux differences are only significant  
615 over industrial/commercial pixels which include buildings with bright roofs (up to ~300 W m<sup>-2</sup>). The  
616 changes in absolute surface albedos do not affect simulated latent heat fluxes as these reflective roofs  
617 are located in industrial/commercial areas with negligible pervious surfaces and simulated latent heat  
618 flux (Fig. 3l).

619 The remote sensing data detect higher LAI values over all pixel types, particularly over fully  
620 vegetated areas where new LAI values are significantly higher (Fig. 3m and 3n). By influencing the  
621 canopy resistance, these changes redefine the spatial distribution of turbulent fluxes (Fig. 3o and 3p).  
622 Over the densely vegetated areas, increases in latent heat flux (up to 50 W m<sup>-2</sup>) and decreases in  
623 sensible heat flux (up to 35 W m<sup>-2</sup>) are found (Fig. 3o and 3p). It is noteworthy that, as illustrated before  
624 (Fig. 3n and 3o), the most significant influences of LAI alterations are detected in the summer months.

**Deleted:** in the default parameterization.

**Deleted:** and higher fluxes over the vegetated areas

**Deleted:** the most

**Deleted:** ; Fig. 3k

**Deleted:** (Fig.

630 Thus, it is not surprising that the turbulent fluxes do not show significant sensitivity to the LAI changes in  
631 April.

632 Remotely sensed emissivity maps, implemented in the Noah-UCM simulations, show minimal  
633 effect on the output turbulent fluxes maps (results not shown). Our results (Fig. 2 and 3) agree with  
634 previous sensitivity studies performed with the Noah-UCM which indicated high sensitivity of the model  
635 to GVF, ISA, albedo, and LAI, and less model sensitivity to emissivity [Loridan et al., 2010; Wang et al.,  
636 2011]. Loridan et al. [2010] highlighted the critical role of ISA and LAI in the simulations of latent heat  
637 flux and albedo role in the sensible heat flux simulations. Investigating the peaks of diurnal turbulent  
638 fluxes, Wang et al. [2011] reported that latent heat flux is the most sensitive to the GVF. They also found  
639 that emissivity has minimal effects on the model outputs.

640

## 641 7. Evaluation of Noah-UCM Performance

642 After initial sensitivity tests, the model performance in reproducing ET and LST fields is evaluated using  
643 remotely sensed (independent from derived parameters) and in situ measurements. The comparisons of  
644 observed and simulated ET and LST, using different urban surface parameterizations (scenarios 1, 7, 8,  
645 and 9 in Table 1), are presented in figures 4, 5, and 6.

### 646 7.1. ET Simulations

647 The temporal variations of ET, simulated by the Noah-UCM model and averaged over fully vegetated  
648 pixels, are evaluated against CIMIS-based ET measurements, spanning 2010 and 2011 (Fig. 4). The  
649 presented observations are averages over fully vegetated pixels in the study domain, calculated using ET  
650 maps based on  $ET_0$  measurements from ten CIMIS stations, landscape coefficients, and inverse-distance  
651 weighting (2<sup>nd</sup> power) (see section 5.2). The model reproduces similar ET behaviors when the default  
652 parameters and the second group of remotely sensed parameters (albedo, LAI, and Emissivity) are  
653 implemented (Fig. 4a and 4c). The ET differences between observations and the default simulation are

Deleted: 4).

655 minimal in the winter and fall months, due to the limited energy available for ET in those months. Over  
656 the warmer months, the observed and modeled ETs show distinct behaviors. CIMIS stations report two  
657 peaks, one in the spring and one in the summer time. Simulated ETs, however, illustrate one peak in the  
658 July. The Noah-UCM, using these parameterizations, underestimates ET rates for the most of winter and  
659 spring months and overestimates them in the summer time (Fig. 4a and 4c). Including remotely sensed  
660 albedo, LAI, and emissivity does not change the general seasonal pattern deviations of ET (Fig. 4a and  
661 4c), but it reduces the biases considerably (with  $R^2=0.83$  and  $RMSE=14.32$  mm/month). We note that  
662 model improvement is mostly associated with inclusion of remotely-sensed LAI maps in the model since  
663 albedo and emissivity have minimal influence on latent heat fluxes from heavily vegetated pixels (see  
664 Fig. 2j).

665 The new GVF and ISA values alter ET seasonal fluctuations significantly in scenario 7 (Fig. 4b). In  
666 agreement with CIMIS observations, the model with inclusion of remotely sensed parameters results in  
667 significantly higher ET values in the warming months (Feb.-May) and lower ETs in the summer time.  
668 Noting that ISA has minimal effects over the fully vegetated pixels, one explanation for this pattern is  
669 that higher green vegetation fraction detected by Landsat in late winter and early spring, increases  
670 transpiration rates as soon as the required energy is available and lower measured GVFs in the summer  
671 time suppresses the transpiration rates, resulting in the lower ET values. These changes enhance the  
672 model performance significantly (with  $R^2=0.92$  and  $RMSE= 11.77$  mm/month).

673 Including all the measured parameter sets (Fig. 4d), reduces the behavioral disagreements  
674 between observed and modeled monthly ET ( $R^2=0.86$ ). Large biases over the summer months are also  
675 reduced. However, ET values are overestimated over the rest of the year ( $RMSE=17.49$  mm/month).  
676 Although each newly developed parameter group enhances the model performance in predicting ET, the  
677 advantages are countered when all of the parameters are implemented in the model. This is possibly  
678 due to the complex interactions between the parameters (e.g. GVF and LAI) in the model structure.

679 A notable pattern detected by CIMIS data is the drop in ET values over the month of June. The sudden  
680 decrease in ET corresponds to the June Gloom weather pattern in southern California, when onshore  
681 flows result in persistent overcast skies with cool temperatures, as well as fog and drizzle in late spring  
682 and early summer [NWS, 2011]. The June Gloom effects are captured in scenarios 7 and 9 (Fig. 4b and  
683 4d) and not seen in scenarios 1 and 8 (Fig. 4a and 4c). Since ISA has minimal influence on ET from the  
684 fully vegetated pixels and the second group fails to simulate June Gloom influence, the improvements in  
685 scenarios 7 and 9, in capturing this phenomenon, are associated with a more accurate representation of  
686 GVF.

## 687 7.2. LST Simulations

688 In order to further evaluate model performance and examine the impacts of different remote sensing  
689 based parameter sets, Landsat-based LST measurements are utilized (Fig. 5 and 6). Statistics ( $R^2$  and  
690 RMSE) are also included to quantify the model performance using different urban surface  
691 parameterizations (Fig. 5). The observed LSTs, over fully vegetated pixels, are estimated with fair

692 accuracy by the default model ( $R^2=0.86$  and  $RMSE=3.21$  °C; Fig 5a). The model performance has almost  
693 the same level of accuracy over low intensity residential areas and is slightly worse (<1°C) over  
694 industrial/commercial pixels (Fig. 5e). Using remote sensing data over fully vegetated and low intensity  
695 residential pixels weakly improves the biases (with <1°C improvement; Fig. 5b-d and 5f-h). Over  
696 industrial/commercial areas, a systematic underestimation of the observed LST is identified ( $RMSE=3.96-$   
697  $4.59$ °C; Fig. 5i-l) which seems to be persistent after using different remotely sensed parameter sets. We  
698 speculate that this underestimation of LST over highly developed areas is due to lack of representation  
699 of anthropogenic heating in the current study.

700 A comparison of LST at 1100 LST on 14 April 2011 with four simulation cases is also presented  
701 (Fig. 6). Alterations due to use of remote sensing products are more noticeable in this spatial  
702 examination of the results. Using all the default parameters (scenario 1), observed LST is overestimated

**Deleted:** is slightly worse (~1°C)

**Deleted:**  $R^2=0.62$  and

**Deleted:** 6.15

**Deleted:** ). Both

**Deleted:** groups (scenarios 7 and 8) significantly improve the correlations between the observed and simulated LSTs (RMSE of 0.76 and 0.70, respectively; Fig. 5j and 5k). When all the parameters are used (scenario 9), the RMSE is enhanced to 0.82. However, the cold biases are persistent in all simulations, more significantly over

**Deleted:** surfaces (Fig. 5e-l).

**Deleted:** Further analysis (not shown here) indicates that underestimation of LST values is due to a fundamental problem in the UCM and cannot be immediately solved with available parameter choices. This problem is discussed in a related study investigating different schemes for LST and conductive heat fluxes in the UCM [Wang et al. 2011b]. Their study shows that the current UCM formulation results in a phase lag and cold biases in simulated surface temperature when compared to observations. The discussed cold biased could potentially be resolved utilizing a spatially-analytical scheme introduced by Wang et al. [2011b]. ¶

723 over the heavily vegetated areas and underestimated over highly developed pixels (Fig. 6a and 6b).  
724 Remotely sensed GVF and ISA (in scenario 7) significantly decrease LSTs over fully vegetated and low  
725 intensity residential pixels and increase temperatures over industrial and commercial areas, resulting in a  
726 better match with the observed LST map. The decreased simulated surface temperatures over heavily  
727 vegetated areas is due to higher GVF and consequently higher ET rates, which in turn lead to lower  
728 sensible heat flux and LSTs (see Fig. 3b). The increased LSTs over highly developed areas is likely due to  
729 lower GVF and higher ISA values detected in Landsat imagery, compared with the default values, which  
730 partition net radiation more into sensible heat flux (see Fig. 3b and 3f). The noticed changes in LST maps,  
731 using remotely sensed albedo, LAI, and emissivity (scenario 8), are small (compare Fig. 6a and 6e).  
732 Although simulated LSTs over fully vegetated areas are decreased, the observed temperatures are still  
733 overestimated (Fig. 6f). The LST decreases in scenario 8 may be explained by evaporative cooling effect  
734 of the higher LAI values over heavily vegetated areas (see Fig. 3n). Similar to scenario 7, considerable  
735 GVF induced LST reductions, over fully vegetated areas, improve the observed LST estimations in  
736 scenario 9 (Fig. 6h). Our assessment indicates that implemented satellite derived parameter maps,  
737 particularly GVF and ISA used in scenarios 7 and 9, enhance the Noah-UCM capability to reproduce the  
738 LST differences between fully vegetated pixels and highly developed areas (simulated LST differences of  
739 3.07, 6.78, 3.48, and 7.30 °C for scenarios 1, 7, 8, and 9 vs. observed LST difference of 11.25 °C).

**Deleted:** result

**Deleted:** However the model still underestimates the observed LSTs over the industrial and commercial pixels (Fig. 6b and 6e).

### 740 **7.3. Energy and Water Budget Evaluation**

741 Differences in the simulated energy and water budgets, with different surface parameterizations  
742 (scenarios 1, 7, 8, and 9 in the Table 1) are summarized for WY 2011 (Fig. 7). The emissivity induced  
743 changes to the energy and water budgets are insignificant and not included. The illustrated radiative and  
744 turbulent heat fluxes show that, unlike the longwave radiative fluxes, the simulated available solar  
745 radiations are altered considerably using different urban parameter sets (up to %6), particularly over  
746 fully vegetated (Fig. 7a) and industrial/commercial pixels (Fig. 7c). These changes are induced by new

**Deleted:** 1.31, 4.81, 1.55

**Deleted:** 4.93

**Deleted:** Nevertheless, the model still underestimates remotely sensed LST values, by about 9.91 °C for scenario 9, over the highly developed areas.

**Deleted:** Regardless of the parameterization processes, cold biases are persistent in all simulations, particularly over high intensity residential and industrial/commercial pixels (Fig. 6). As explained above, this underestimation of LST values is consistent with the literature and is reported to be due to a fundamental problem in the UCM which produces a phase lag and cold biases in simulated LST [Wang et al., 2011b]. ¶

762 surface albedo values utilized in scenarios 8 and 9. It is also observed that most of the incoming  
763 radiative energy is dissipated through latent heat fluxes, over heavily vegetated pixels (Fig. 7a and 7b),  
764 and sensible heat fluxes over industrial/commercial areas (Fig. 7c). These turbulent fluxes are also  
765 altered when different surface parameterizations are incorporated. Implementing all the remotely  
766 sensed parameters (scenario 9), the annual latent heat flux is increased (12%) over fully vegetated pixels  
767 (Fig. 7a), and the annual sensible heat flux is decreased (32%) over industrial/commercial pixels (Fig. 7c).  
768 Ground heat fluxes, however, are insignificant and unchanged.

769 Water budget terms also show variable behavior using different parameter sets over different  
770 land cover types (Fig. 7 d-f). Annual irrigation amounts exceed received precipitations over the pixels  
771 with significant vegetation fractions (Fig. 7d and 7e). This pattern is not rare in semi-arid regions [CDWR  
772 1975, Mini et al., 2014]. In these areas, most of incoming water is lost through ET (Fig. 7d and 7e). Areas  
773 with high coverage of impervious surfaces, however, dissipate most of the incoming moisture through  
774 surface runoff (Fig. 7f). The alterations in the annual ET rates are, for the most part, due to the changes  
775 in the GVF parameterizations (scenarios 7 and 9; Fig. 7d-f). Sub-surface runoff annual rates, on the other  
776 hand, are altered using new ISA values (scenarios 7 and 9; Fig. 7e and 7f). Changes in the annual ET  
777 values are as large as 145, 156, and 79.4 mm over fully vegetated, low intensity residential and  
778 industrial/commercial pixels, respectively (Fig. 7d-f).

779 To further verify the capability of Noah-UCM to reproduce observed ET quantities, additional  
780 evaluation of the model is conducted utilizing ground-based chamber ET measurements in the greater  
781 Los Angeles area [Moering, 2011]. Instantaneous ET measurements, over an irrigated park in the study  
782 domain during WY 2011, are converted to daily and then annual ET estimates (1224 mm) and compared  
783 with the simulated ET values over the parks (Fig. 7d). As expected, the observed ET is best reproduced  
784 by scenario 7 (Bias of 1.47 mm) due to more accurate representation of GVF in the model. Scenarios 1  
785 (with the default parameters) and 8 underestimate, with biases of 58.65 and 65.32 mm, respectively.



786 Scenario 9, with all the remotely sensed parameters, overestimates the measured ET (with bias of 86.24  
787 mm). These shortcomings are likely due to: (1) a lack of accurate representation of GVF in the default  
788 parameter sets, used in scenarios 1 and 8, (2) the uncertainties associated with the estimated LAI values  
789 utilized in scenarios 8 and 9, and (3) complex interactions between GVF and LAI noted in scenario 9.  
790 The presented analysis of energy balance (Fig. 7) suggests that GVF, albedo and LAI play an important  
791 role in regulating simulated radiative energy budget and turbulent fluxes, mainly by affecting the  
792 available net radiation and transpiration quantities. GVF, ISA, and LAI also alter the study area  
793 transpiration and ET values, as well as surface runoff rates.

794

## 795 **8. Conclusions**

796 In the current work we investigate the utility of a select set of remote sensing based surface parameters  
797 in the Noah-UCM modeling framework over a highly developed urban area. It was found that remote  
798 sensing data show significantly different magnitudes and seasonal patterns of GVF when compared with  
799 the default values. The reason for this mismatch is the significant and year round irrigation in the Los  
800 Angeles area which is not accounted for in the default parameter tables. Irrigated landscapes maintain  
801 constant greenness rather than a seasonal behavior of greening in the winter/spring and browning in  
802 the summer. The noticed differences between the monthly LAI values from default tables and remotely  
803 sensed data are also due to complex irrigation patterns. Another factor that contributes to this  
804 mismatch is the fact that landscape plantings are quite different from agricultural crops due to their  
805 being composed of collections of vegetation species which is not taken into account in the vegetation  
806 parameter tables in the Noah LSM [CDWR, 2000; Vahmani and Hogue, 2013; 2014]. There are also  
807 considerable deviations between the look-up-table-based ISA, albedo and emissivity maps and the  
808 remotely sensed values. The results of our analysis agree with previous studies which show high  
809 sensitivity of the Noah-UCM to GVF, ISA, albedo, and LAI, and minimal model sensitivity to emissivity

810 [Loridan et al., 2010; Wang et al., 2011]. Our results show that GVF, ISA and LAI are critical in the  
811 simulations of latent and sensible heat flux, and that albedo plays a key role in the sensible heat flux  
812 simulations.

813 Our assessment of the Noah-UCM ET estimation shows that using the default parameters leads  
814 to significant errors in the model predictions of monthly ET fields (RMSE= 22.06 mm/month) over the  
815 study domain in Los Angeles. Results show that accurate representation of GVF is critical to reproduce  
816 observed ET patterns over vegetated areas in the urban domains. LAI also plays an important role in ET  
817 simulations. However, simulations incorporating the remotely sensed GVF values outperform (RMSE=  
818 11.77 mm/month) simulations with the new LAI estimates (RMSE=14.32 mm/month). This could be due  
819 to several reasons. First, there are uncertainties associated with the remote sensing based LAI retrieval,  
820 including non-linearity of LAI-vegetation index (RSR) relationships [Latifi and Galos, 2010], which do not  
821 apply to NDVI-based GVF. Second, more accurate representation of GVF values in the Noah-UCM not  
822 only improves the assigned LAI values to the vegetated pixels in the model but also enhances other  
823 parameters inputs as well (i.e. albedo, emissivity, and roughness length). Further analysis of the model  
824 performance indicates that implemented satellite derived parameter maps, particularly GVF and ISA,  
825 enhance the Noah-UCM capability to reproduce the LST differences between fully vegetated pixels and  
826 highly developed areas (simulated LST differences of 3.07 and 6.78 °C for scenarios with default and  
827 remotely sensed GVF and ISA vs. observed LST difference of 11.25 °C).

828 Our analysis of energy balance suggests that GVF, albedo and LAI play an important role in  
829 regulating simulated radiative energy budget and turbulent fluxes, mainly by affecting the available net  
830 radiation and ET quantities. With regard to urban water balance, GVF, ISA, and LAI play a key role in  
831 surface hydrologic fluxes, including ET and surface runoff. When compared with in-situ observations,  
832 Noah-UCM shows the capacity to reproduce ET fields with relatively high accuracy (Bias of 1.47 mm)  
833 when GVF maps are updated using remote sensing data.

Deleted: 1.31

Deleted: 4.81

Deleted: Nevertheless, the model still underestimates remotely sensed LST values, over highly developed areas. We speculate that the underestimation of LST values, particularly over high intensity residential and industrial/commercial areas, is due to structural parameterization in the UCM and cannot be immediately solved with available parameter choices.

842 In summary, the current study highlights the significant deviations between the spatial distributions and  
843 seasonal fluctuations of the default and remotely sensed parameter sets in the Noah-UCM. We illustrate  
844 that replacing default parameters with the measured values reduces significant biases in model  
845 predictions of the surface fluxes within irrigated urban areas. This ultimately has key implications in  
846 feedback processes to the atmosphere when the Noah-UCM is coupled with the widely used WRF  
847 model, which has been increasingly applied over urban areas to examine the exchange of heat,  
848 moisture, momentum or pollutants. Semi-arid urban cities, [in particular](#), are receiving much attention in  
849 the literature, given their accelerated growth and increasing dependence on external water sources.  
850 More accurate representation of both water and energy fluxes [in commonly used modeling frameworks](#)  
851 is critical for regional resource management as well as predictions of urban processes under future  
852 climate conditions. [Although this study focuses on the widely used single layer UCM, we speculate that](#)  
853 [implementation of the more accurate remote sensing based parameters \(particularly, GVF and ISA\) may](#)  
854 [also enhance performance of the Noah-BEP \[Martilli et al., 2002\], which is currently the most](#)  
855 [sophisticated urban scheme in WRF. In this multi-layer UCM a similar approach to the single layer UCM](#)  
856 [is used based on an urban fraction \(or ISA\) parameter that couples the Noah outputs over pervious](#)  
857 [portion of pixels and UCM outputs over developed surfaces.](#)

#### 858 **Acknowledgements**

859 Funding for this research was supported by an NSF Hydrologic Sciences Program CAREER Grant  
860 (#EAR0846662), a 2012 NASA Earth and Space Science Fellowship (#NNX12AN63H), and an NSF Water  
861 Sustainability and Climate (WSC) grant (#EAR12040235).

862

863 **References**

864 Arnfield, A. J.: Two decades of urban climate research: A review of turbulence, exchanges of energy and  
865 water, and the urban heat island, *Int. J. Climatol.*, 23: 1–26, doi: 10.1002/joc.859, 2003.

866 Artis, D. A. and Carnahan, W. H.: Survey of emissivity variability in thermography of urban areas, *Remote  
867 Sensing of Environment*, 12, 313–329, 1982.

868 Bauer, M. E., Loeffelholz, B., and Wilson, B.: Estimating and mapping impervious surface area by  
869 regression analysis of Landsat imagery, *Remote Sensing of Impervious Surfaces*, pp. 3–20, Boca Raton,  
870 Florida: CRC Press, 2007.

871 Bornstein, R.: Urban climate models: Nature, limitations, and applications, *Meteorol. Atmos. Phys.*, 38,  
872 185–194, 1987.

873 Burian, S. , Brown, M. J., Augustus, N.: Development and assessment of the second generation National  
874 Building Statistics database, Seventh Symposium on the Urban Environment, San Diego, CA, 10–13  
875 September, American Meteorological Society: Boston, MA, Paper 5.4, 2007.

876 Burian, S. J., Stetson, S. W., Han, W., Ching, J., and Byun, D.: High resolution dataset of urban canopy  
877 parameters for Houston, Texas, Preprint proceedings, Fifth Symposium on the Urban Environment,  
878 Vancouver, BC, Canada, 23–26 August, American Meteorological Society: Boston, MA, 2004.

879 Burian, S., Brown, M., McPherson, T. N., Hartman, J., Han, W., Jeyachandran, I., Rush, J.: Emerging urban  
880 databases for meteorological and dispersion, Sixth Symposium on the Urban Environment, Atlanta, GA,  
881 28 January–2 February, American Meteorological Society: Boston, MA, Paper 5.2, 2006.

Deleted: 9,

883 California Department of Water Resources (CDWR): A guide to estimating irrigation water needs of  
884 landscape plantings in California: The landscape coefficient method and WUCOLS III, [Department of](#)  
885 [Water resources](#), State of California, 1–150, 2000.

886 California Department of Water Resources (CDWR): California’s ground water, bulletin 118, [Department](#)  
887 [of Water resources](#), State of California, 1975.

888 Changnon, S. A. and Huff, F. A.: The urban-related nocturnal rainfall anomaly at St. Louis, J. Climate Appl.  
889 Meteor., 25, 1985–1995, doi:[10.1175/1520-250450\(1986\)025<1985:TURNRA>2.0.CO;2](#), 1986.

890 Changnon, S. A.: Inadvertent weather modification in urban area: Lessons for global climate change.  
891 Bull. Amer. Meteor. Soc., 73, 619–627, doi:[10.1175/1520-0477\(1992\)073<0619:IWMIUA>2.0.CO;2](#),  
892 1992.

893 Chen, F. and Dudhia, J.: Coupling an advanced land-surface/hydrology model with the Penn State/NCAR  
894 MM5 modeling system. Part I: model implementation and sensitivity, Monthly Weather Review, 129:  
895 569–585, 2001.

896 Chen, F., Janjic, Z., and Mitchell, K.: Impact of atmospheric surface layer parameterization in the new  
897 land-surface scheme of the NCEP mesoscale Eta model, Boundary-Layer Meteorology, 85: 391–421,  
898 DOI:[10.1023/A:1000531001463](#), 1997.

899 Chen, F., Kusaka, H., Bornstein, R., Ching, J., Grimmond, C. S. B., Grossman-Clarke, S., Loridan, T.,  
900 Manning, K. W., Martilli, A., Miao, S., Sailor, D., Salamanca, F. P., Taha, H., Tewari, M., Wang, X.,  
901 Wyszogrodzki, A. A., and Zhang, C.: The integrated WRF/urban modelling system: development,  
902 evaluation, and applications to urban environmental problems, Int. J. Climatol., 31: 273–288. doi:  
903 [10.1002/joc.2158](#), 2011.

Deleted: <http://dx.doi.org/>

Deleted: <http://dx.doi.org/>

906 Chen, F., Kusaka, H., Tewari, M., Bao, J. W., Harakuchi, H.: Utilizing the coupled WRF/LSM/urban  
907 modeling system with detailed urban classification to simulate the urban heat island phenomena over  
908 the Greater Houston area, Paper 9.11, American Meteorological Society Fifth Symposium on the Urban  
909 Environment, Vancouver, BC, Canada, 2004.

910 Chen, F., Mitchell, K., Schaake, J., Xue, Y., Pan, H.-L., Koren, V., Duan, Q. Y., Ek, M., Betts, A.: Modeling of  
911 land-surface evaporation by four schemes and comparison with FIFE observations, *J. Geophys. Res.*,  
912 101(D3), 7251–7268, doi:10.1029/95JD02165, 1996.

913 Cheng, F. Y. and Byun, D.W.: Application of High Resolution Land Use and Land Cover Data for  
914 Atmospheric Modeling in the Houston-Galveston Metropolitan Area: Part I, *Meteorological Simulation*  
915 *Results, Atmospheric Environment*, 42, 7795-7811, doi:10.1016/j.atmosenv.2008.04.055, 2008.

916 Cheng, F. Y., Hsu, Y. C., Lin, P. L., Lin, T. H.: Investigation of the Effects of Different Land Use and Land  
917 Cover Patterns on Mesoscale Meteorological Simulations in the Taiwan Area, *J. Appl. Meteor. Climatol.*,  
918 52, 570–587, doi: <http://dx.doi.org/10.1175/JAMC-D-12-0109.1>, 2013.

919 Ching, J., Brown, M., McPherson, T., Burian, S., Chen, F., Cionco, R., Hanna, A., Hultgren, T., Sailor, D.,  
920 Taha, H., Williams, D.: National Urban Database and Access Portal Tool, NUDAPT, *Bulletin of the*  
921 *American Meteorological Society*, 90(8): 1157–1168, DOI:10.1175/2009BAMS2675.1, 2009.

922 Cotton, W. R. and Pielke, R. A.: *Human impacts on weather and climate*. Cambridge: Cambridge  
923 University Press, 1995.

924 De Ridder, K., Bertrand, C., Casanova, G., and Lefebvre, W.: Exploring a new method for the retrieval of  
925 urban thermophysical properties using thermal infrared remote sensing and deterministic modeling, *J.*  
926 *Geophys. Res.*, 117, D17108, doi:10.1029/2011JD017194, 2012.

927 Ek, M. B., Mitchell, K. E., Lin, Y., Rogers, E., Grunmann, P., Koren, V., Gayno, G., Tarpley, J. D.:

928 Implementation of Noah land surface model advances in the National Center for Environmental

929 Prediction operational mesoscale Eta model, *J. Geophys. Res.*, 108, 8851, doi:10.1029/2002JD003296,

930 2003.

931 Giannaros, T. M., Melas, D., Daglis, I. A., Keramitsoglou, I., Kourtidis, K.: Numerical study of the urban

932 heat island over Athens (Greece) with the WRF model, *Atmospheric Environment*, Volume 73, 103-111,

933 doi:10.1016/j.atmosenv.2013.02.055, 2013.

934 Gutman, G. and Ignatov, A.: Derivation of green vegetation fraction from NOAA/AVHRR for use in

935 numerical weather prediction models, *Int. J. Remote Sens.*, 19: 1533-1543, 1998.

936 Hanasaki, N., Kanae, S., Oki, T., Masuda, K., Motoya, K., Shirakawa, N., Shen, Y., and Tanaka, K.: An

937 integrated model for the assessment of global water resources- Part 1: Model description and input

938 meteorological forcing, *Hydrol. Earth Syst. Sci.*, 12, 1007-1025, doi:10.5194/hess-12-1007-2008, 2008a.

939 Hanasaki, N., Kanae, S., Oki, T., Masuda, K., Motoya, K., Shirakawa, N., Shen, Y., and Tanaka, K.: An

940 integrated model for the assessment of global water resources- Part 2: Applications and assessments,

941 *Hydrol. Earth Syst. Sci.*, 12, 1027-1037, doi:10.5194/hess-12-1027-2008, 2008b.

942 Jiang, X., Wiedinmyer, C., Chen, F., Yang, Z. L., and Lo, J. C. F.: Predicted impacts of climate and land use

943 change on surface ozone in the Houston, Texas, area, *J. Geophys. Res.*, 113, D20312,

944 doi:10.1029/2008JD009820, 2008.

945 Jin, M. and Shepherd J. M.: Inclusion of urban landscape in a climate model—How can satellite data

946 help?, *Bull. Am. Meteorol. Soc.*, 86(5), 681–689, DOI:10.1175/BAMS-86-5-681, 2005.

947 Johnson, T. D. and Belitz K.: A remote sensing approach for estimating the location and rate of urban

948 irrigation in semi-arid climates, *Journal of Hydrology*, 414-415, 86-98, 2012.

949 Justice, C. O., Townshend, J. R. G., Vermote, E. F., Masuoka, E., Wolfe, R. E., Saleous, N., Roy, D. P.,  
950 Morisette, J. T.: An overview of MODIS land data processing and product status. *Remote Sensing of*  
951 *Environment*, 83(1–2), 3–15, 2002.

952 Kalnay, E. and Cai, M.: Impact of urbanization and land-use change on climate, *Nature*, 423(29),  
953 528–531, 2003.

954 Kusaka, H., Kimura, F.: Thermal effects of urban canyon structure on the nocturnal heat island: Numerical  
955 experiment using a mesoscale model coupled with an urban canopy model, *J. Appl. Meteorol.* 43: 1899–  
956 1910, 2004.

957 Kusaka, H., Kondo, H., Kikegawa, Y., and Kimura, F.: A simple single-layer urban canopy model for  
958 atmospheric models: Comparison with multi-layer and slab models, *Bound.-Layer Meteorol.*, 101, 329–  
959 358, 2001.

960 Landsberg, H. E.: *The urban climate*. New York: Academic Press, 1981.

961 Latifi, H. and Galos, B.: Remote sensing-supported vegetation parameters for regional climate models: a  
962 brief review, *iForest* 3: 98-101, doi: 10.3832/ifor0543-003, 2010.

963 Loridan, T., Grimmond, C. S. B., Grossman-Clarke, S., Chen, F., Tewari, M., Manning, K., Martilli, A.,  
964 Kusaka, H., Best, M.: Trade-offs and responsiveness of the single-layer urban parameterization in WRF:  
965 an offline evaluation using the MOSCEM optimization algorithm and field observations, *Q.J.R. Meteorol.*  
966 *Soc.*, 136: 997–1019. doi: 10.1002/qj.614, 2010.

967 Lowry, W.: Urban effects on precipitation amount, *Progress in Physical Geography*, 22(4), 477–520, DOI:  
968 10.1177/030913339802200403, 1998.



969 Marshall, C. H., Pielke, R. A., Steyaert, L., and Willard, D.: The impact of anthropogenic land-cover  
970 change on the Florida peninsula sea breezes and warm season sensible weather, *Mon. Wea. Rev.*, 132,  
971 28–52, doi: <http://dx.doi.org/10.1175/1520-0493>, 2004.

972 [Martilli, A., Clappier, A., and Rotach, M. W.: An urban surface exchange parameterization for mesoscale](#)  
973 [models, \*Boundary-Layer Meteorology\* 104: 261–304, 2002.](#)

974 McPherson, E. G., Simpson, J. R., Xiao, Q., Wu, C.: Los Angeles 1-million tree canopy cover assessment,  
975 Gen. Tech. Rep. PSW-GTR-207, Albany, CA: U.S. Department of Agriculture, Forest Service, Pacific  
976 Southwest Research Station, 52 p, 2008.

977 Miao, S. and Chen F.: Formation of horizontal convective rolls in urban areas, *Atmospheric Research*,  
978 89(3): 298–304, doi:10.1016/j.atmosres.2008.02.013, 2008.

979 Miao, S., Chen F., LeMone, M. A., Tewari M., Li, Q., Wang, Y.: An observational and modeling study of  
980 characteristics of urban heat island and boundary layer structures in Beijing, *J. Appl. Meteor. Climatol.*,  
981 48, 484–501, doi: <http://dx.doi.org/10.1175/2008JAMC1909.1>, 2009.

982 Mini, C., Hogue, T. S., ~~and~~ Pincetl, S.: Estimation of Residential Outdoor Water Use in Los Angeles,  
983 California, Landscape [Urban Plan](#), 127, 124–135, doi:10.1016/j.landurbplan.2014.04.007, 2014.

Deleted: ., 2014:

Deleted: and Urban Planning (in press)

984 Moering, D. C.: A comparative study of evapotranspiration rates between irrigated and non-irrigated  
985 parks in Los Angeles, M.S. thesis, Dep. of Civil and Env. Eng., Univ. of California Los Angeles, Los Angeles,  
986 California, 2011.

987 National Oceanographic and Atmospheric Administration-Coastal Services Center (NOAA-CSC): Southern  
988 California 2000-Era Land Cover/Land Use, LANDSAT-TM, 10m, NOAA-CSC, Charleston, SC, 2003.

991 National Weather Service (NWS): Jet Stream - The Marine Layer, NOAA National Weather Service,  
992 <http://www.srh.noaa.gov/jetstream/ocean/marine.htm> (last access: 24 February 2013), 2011.  
993 Niyogi, D., Holt, T., Zhong, S., Pyle, P. C., and Basara, J.: Urban and land surface effects on the 30 July  
994 2003 mesoscale convective system event observed in the Southern Great Plains, *J. Geophys. Res.*, 111,  
995 D19107, doi:10.1029/2005JD006746, 2006.

996 Pielke, R. A. Sr., Marland, G., Betts, R. A., Chase, T. N., Eastman, J. L., Niles, J. O., Niyogi, D., and Running,  
997 S.: The influence of land-use change and landscape dynamics on the climate system: Relevance to  
998 climate change policy beyond the radiative effect of greenhouse gases, *Phil. Trans. R. Soc. London A*,  
999 360(Special Theme Issue), 1705–1719, 2002.

1000 Pokhrel, Y., Hanasaki, N., Koirala, S., Cho, J., Kim, H., Yeh, P. J.-F., Kanae, S., and Oki, T.: Incorporating  
1001 anthropogenic water regulation modules into a land surface model, *Journal of Hydrometeorology*, 13  
1002 (1), 255-269, doi: 10.1175/JHM-D-11-013.1, 2012.

1003 Sailor, D. J., Lu, L.: A top-down methodology for developing diurnal and seasonal anthropogenic heating  
1004 profiles for urban areas, *Atmospheric Environment* 38: 2737–2748,  
1005 doi:10.1016/j.atmosenv.2004.01.034, 2004.

1006 Schaaf, C. B., Gao, F., Strahler, A. H., Lucht, W., Li, X. W., Tsang, T., Strugnell, N. C., Zhang, X. Y., Jin, Y. F.,  
1007 Muller, J. P., Lewis, P., Barnsley, M., Hobson, P., Disney, M., Roberts, G., Dunderdale, M., Doll, C.,  
1008 d'Entremont, R. P., Hu, B. X., Liang, S. L., Privette, J. L., Roy, D.: First operational BRDF, albedo nadir  
1009 reflectance products from MODIS, *Remote Sensing of Environment*, 83(2-Jan), 135-148, 2002.

1010 Shuai, Y., Masek, J. G., Gao, F., and Schaaf, C. B.: An algorithm for the retrieval of 30-m snow-free albedo  
1011 from Landsat surface reflectance and MODIS BRDF, *Remote Sensing of Environment*, 115, 2204-2216,  
1012 doi:10.1016/j.rse.2011.04.019, 2011.

Deleted: ,

1014 Shuai, Y., Schaaf, C. B., Strahler, A. H., Liu, J., and Jiao, Z.: Quality assessment of BRDF/albedo retrievals  
1015 in MODIS operational system, *Geophysical Research Letters*, 35, L05407, 5PP,  
1016 doi:10.1029/2007GL032568, 2008.

1017 Sobrino, J. A. and Raissouni, N.: Toward remote sensing methods for land cover dynamic monitoring:  
1018 Application to Morocco, *International Journal of Remote Sensing*, 21, pp. 353–366  
1019 DOI:10.1080/014311600210876, 2000.

1020 Sobrino, J. A., Raissouni, N., and Li, Z. L.: A comparative study of land surface emissivity retrieval from  
1021 NOAA data. *Remote Sensing of Environment*, 75, pp. 256–266, 2001.

1022 Song, M. and Civco, D. L.: A knowledge-based approach for reducing cloud and shadow, *Proceedings of*  
1023 *the American Society of Photogrammetry and Remote Sensing annual convention*, Washington, DC:  
1024 *American Society of Photogrammetry and Remote Sensing*, 7 p, 2002.

1025 State of California Department of Water Resources (SCDWR): California irrigation management  
1026 information system, Sacramento, CA: State of California Department of Water Resources, Available at:  
1027 <http://www.water.ca.gov/>, 2009.

1028 Stathopoulou, M. and Cartalis, C.: Daytime urban heat islands from Landsat ETM+ and Corine land cover  
1029 data: An application to major cities in Greece, *Solar Energy*, 81 (3), pp. 358-368,  
1030 doi:10.1016/j.solener.2006.06.014, 2007.

1031 Stathopoulou, M., Cartalis, C., and Petrakis, M.: Integrating Corine Land Cover data and Landsat TM for  
1032 surface emissivity definition: application to the urban area of Athens, Greece, *International Journal of*  
1033 *Remote Sensing*, 28:15, 3291-3304, DOI:10.1080/01431160600993421, 2007.

1034 Stenberg, P., Rautiainen, M., Manninen, T., Voipio, P., and Smolander, H.: Reduced simple ratio better  
1035 than NDVI for estimating LAI in Finnish pine and spruce stands, *Silva Fennica* 38(1): 3–14, 2004.

1036 Taha, H., Ching, J. K. S.: UCP/MM5 Modeling in conjunction with NUDAPT: model requirements, updates,  
1037 and applications, Seventh Symposium on the Urban Environment, San Diego, CA, 10–13 September,  
1038 American Meteorological Society: Boston, MA, Paper 6.4, 2007.

1039 Taha, H., Douglas, S., and Haney, J.: Mesoscale meteorological and air quality impacts of increased urban  
1040 albedo and vegetation, *Energy and Buildings*, 25, 169–177, DOI: 10.1016/S0378-7788(96)01006-7, 1997.

1041 Taha, H.: Meso-urban meteorological and photochemical modeling of heat island mitigation,  
1042 *Atmospheric Environment*, 42: 8795–8809, DOI:10.1016/j.atmosenv.2008.06.036, 2008.

1043 Taha, H.: Modifying a mesoscale meteorological model to better incorporate urban heat storage: a bulk-  
1044 parameterization approach, *J. Appl. Meteorol.*, 38, 466–473, doi:10.1175/1520-  
1045 0450(1999)038<0466:MAMMMT>2.0.CO;2, 1999.

1046 Tan, M. and Li, X.: Integrated assessment of the cool island intensity of green spaces in the mega city of  
1047 Beijing, *International Journal of Remote Sensing*, 34:8, 3028-3043, DOI:  
1048 10.1080/01431161.2012.757377, 2013.

1049 Tewari, M., Kusaka, H., Chen, F., Coirier, W. J., Kim, S., Wyszogrodzki, A., Warner, T. T.: Impact of  
1050 coupling a microscale computational fluid dynamics model with a mesoscale model on urban scale  
1051 contaminant transport and dispersion, *Atmospheric Research* 96: 656–664,  
1052 doi:10.1016/j.atmosres.2010.01.006, 2010.

1053 US Census: US Census Bureau Releases Data on Population Distribution and Change in the US Based on  
1054 Analysis of 2010 Census Results, US Census Bureau, 24 March 2011.

1055 Vahmani, P. and Hogue, T. S.: Modelling and analysis of the impact of urban irrigation on land surface  
1056 fluxes in the Los Angeles metropolitan area, *Climate and Land Surface Changes in Hydrology Proceedings*  
1057 of H01, IAHS-IAPSO-IASPEI Assembly, Gothenburg, Sweden, July 2013, IAHS Publ. 359, 2013.

Deleted: Meteor

Deleted: http://dx.doi.org/

Deleted: U.S.

Deleted: U.S.

Deleted: U.S.

Deleted: U.S.

Deleted: 24,

1065 Vahmani, P. and Hogue, T. S.: Incorporating an Urban Irrigation Module into the Noah Land Surface  
1066 Model Coupled with an Urban Canopy Model, [J. Hydrometeorol.](#), doi:10.1175/JHMD-13-0121.1, in press,  
1067 [2014](#).

1068 Van Wevenberg, K., De Ridder, K., Van Rompaey, A.: Modeling the contribution of the Brussels heat  
1069 island to a long temperature time series, *Journal of Applied Meteorology and Climatology*, 47, 976e990,  
1070 DOI: 10.1175/2007JAMC1482.1, 2008.

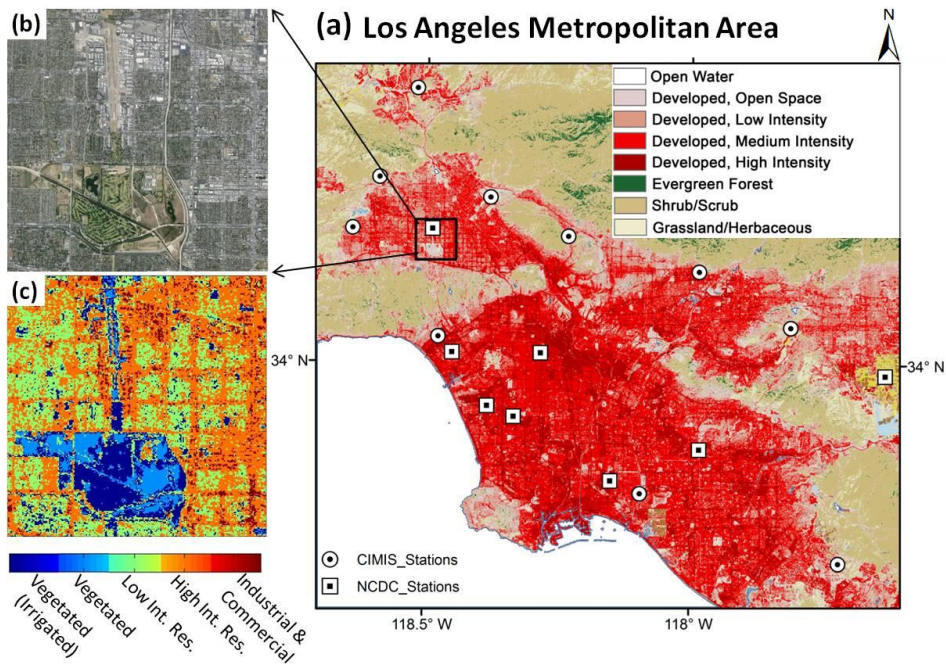
1071 Wang, X. M., Chen, F., Wu, Z. Y., Zhang, M. G., Tewari, M., Guenther, A., and Wiedinmyer, C.: Impacts of  
1072 weather conditions modified by urban expansion on surface ozone: comparison between the Pearl River  
1073 Delta and Yangtze River Delta regions, *Adv. Atmos. Sci*, 26(5), 962-972, doi: 10.1007/s00376-009-8001-2,  
1074 2009.

1075 Wang, Z. H., Bou-Zeid, E., Au, S. K., and Smith, J. A.: Analyzing the sensitivity of WRF's single-layer urban  
1076 canopy model to parameter uncertainty using advanced Monte Carlo simulation, *J. Appl. Meteor.*  
1077 *Climatol.*, 50, 1795–1814, doi: <http://dx.doi.org/10.1175/2011JAMC2685.1>, 2011.

1078 Wei-guang, M., Yan-xia, Z., Jiang-nan, L., Wen-shi, L., Guang-feng, D., and Hao-ru, L.: Application of  
1079 WRF/UCM in the simulation of a heat wave event and urban heat island around Guangzhou, *Journal of*  
1080 *Tropical Meteorology*, 03, 257-267, doi: 10.3969/j.issn.1006-8775.2011.03.007, 2011.

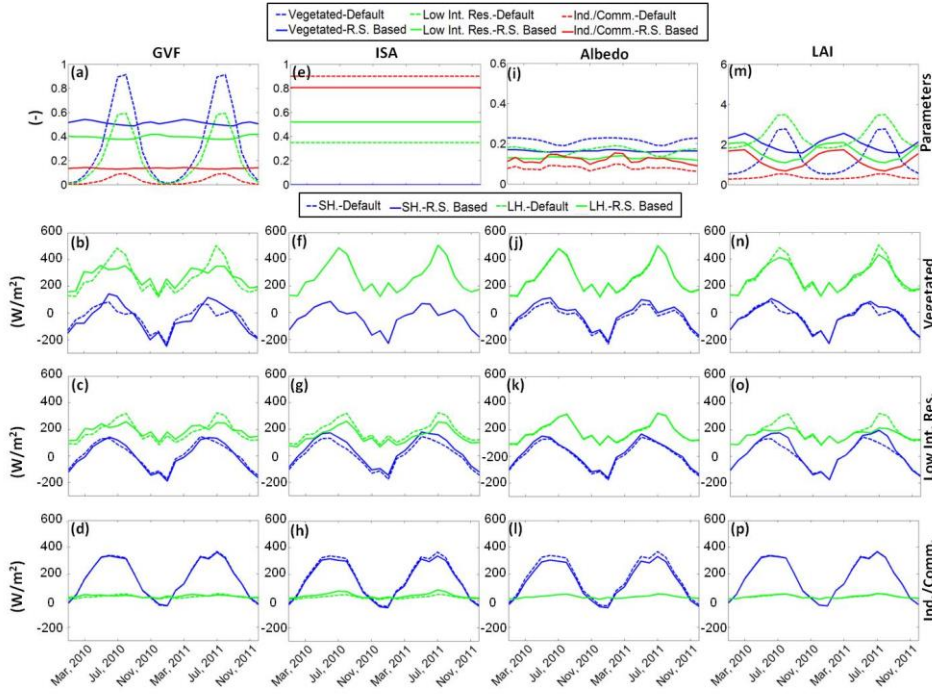
1081

**Deleted:** Journal of Hydrometeorology, 2014 (in press).



1085 **Figure 1.** (a) NOAA C-CAP Land cover map of the Los Angeles metropolitan area including study domain, 10  
 1086 CIMIS stations (white circles), and 8 NCDC stations (white squares), (b) Google image of the study domain, and  
 1087 (c) The Noah/UCM urban land cover classification of the study domain.

Deleted: 1



1098

1099

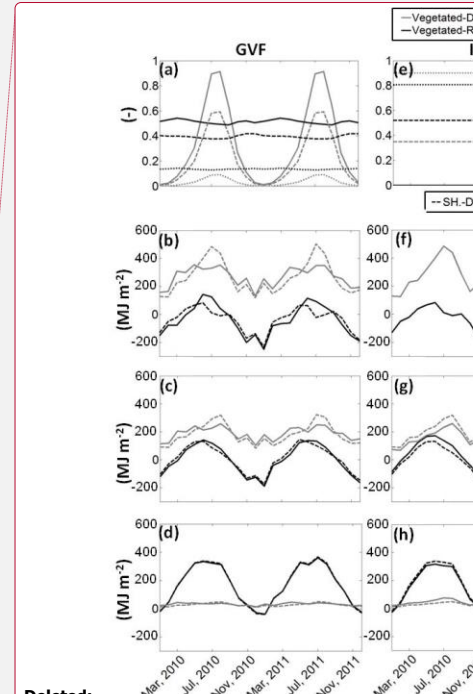
1100

1101

1102

1103

Figure 2. Monthly time series of default Noah/UCM compared with remote sensing based GVF, ISA, albedo, and LAI (row 1) and modeled cumulative monthly sensible and latent heat fluxes ( $\text{MJ m}^{-2}$ ) over fully vegetated, low intensity residential, and industrial/commercial areas using the default and newly estimated parameters: (b-d) GVF, (f-h) ISA, (j-l) albedo, and (n-p) LAI.



Deleted:

Deleted: 2

Deleted: a, e, i, and m

Deleted: ,



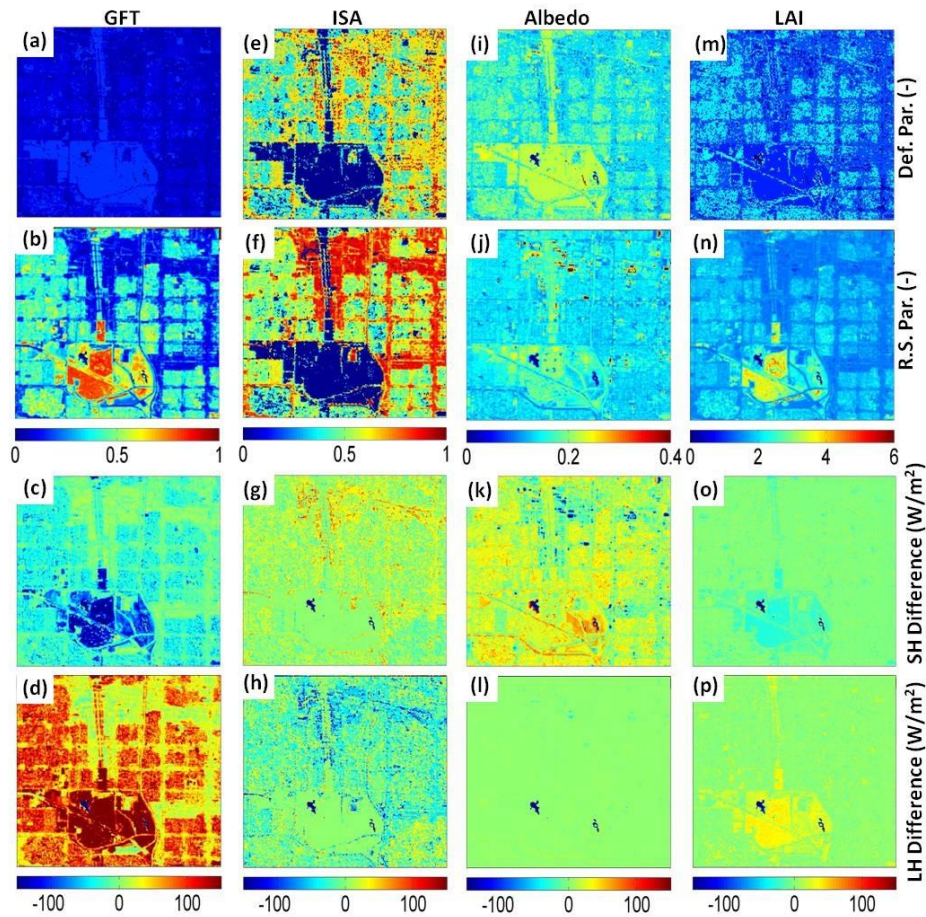
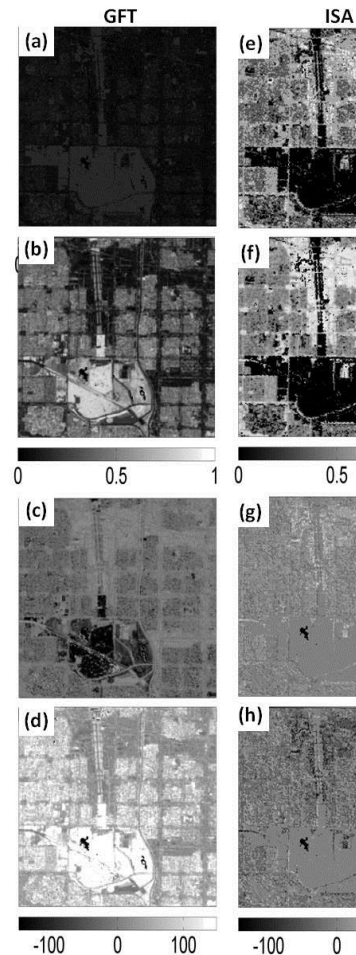


Figure 3. Spatial distributions of GVF, ISA, albedo, and LAI based on Noah/UCM lookup tables (row 1) compared with remotely sensed values (row 2) and simulated difference maps of sensible (row 3) and latent (row 4) heat fluxes using default and remotely sensed urban surface parameters: (c and d) GVF, (g and h) ISA, (k and l) albedo, and (o and p) LAI. Valid at 1100 LST on 14 April 2011.



Deleted:

Deleted: 3

Deleted: remote sensing based

Deleted: (a, e, i, and m) compared with those

Deleted: b, f, j, and n

Deleted: turbulent

1108

1109

1110

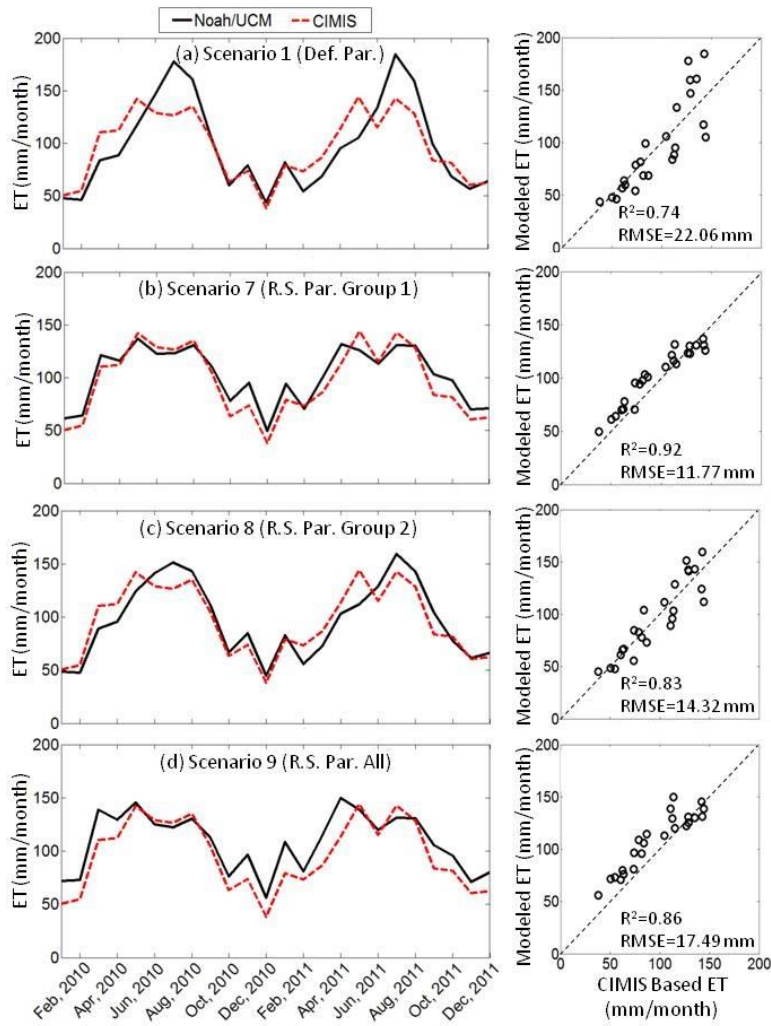
1111

1112

1113

1114



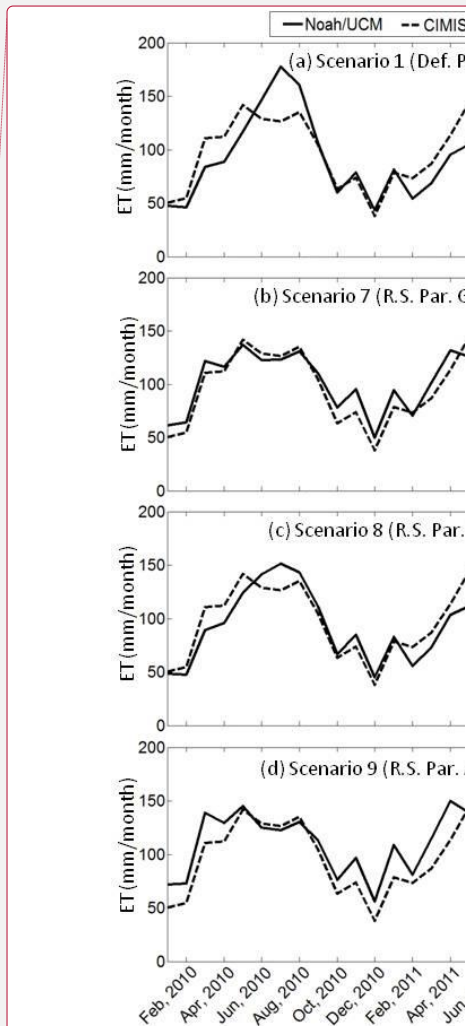


1121

1122 **Figure 4.** Noah/UCM simulated cumulative monthly ET, averaged over fully vegetated pixels using different  
 1123 urban surface parameterizations: scenarios (a) 1, (b) 7, (c) 8, and (d) 9 in the table 1 and their comparisons with  
 1124 CIMIS-based ET measurements spanning 2010 and 2011. Scatter plots of these comparisons are also included  
 1125 (right).

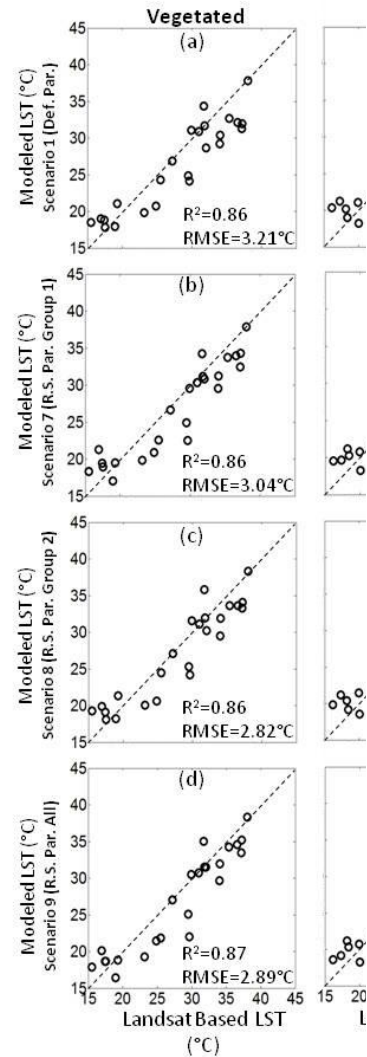
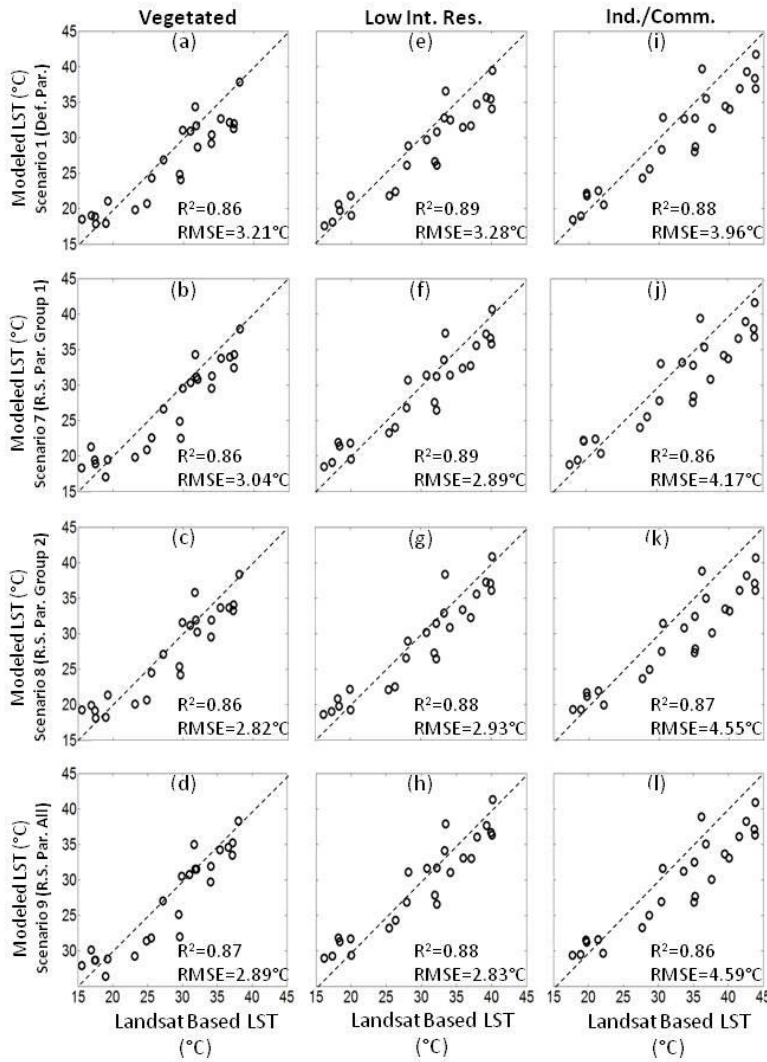
1126

1127



Deleted:

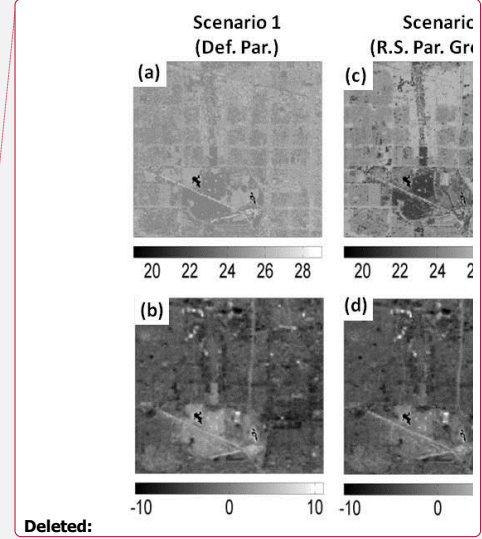
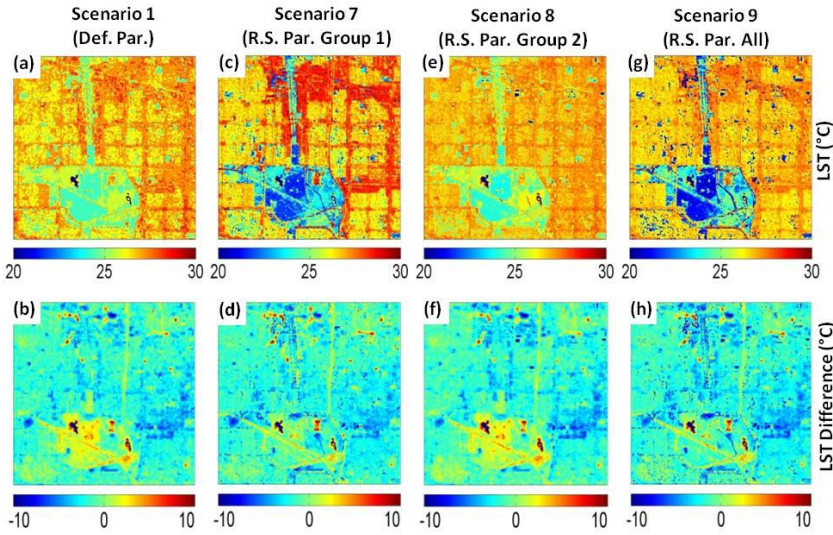
Deleted: 4



Deleted:  
 Deleted:  
 Deleted: 5

Figure 5. Scatter plots of observed (Landsat-based) versus simulated LSTs averaged over different land cover types using different urban surface parameterizations, including scenarios 1 (first row), 7 (second row), 8 (third row), and 9 (forth row) in Table 1.

1130  
 1131  
 1132  
 1133  
 1134



Deleted:

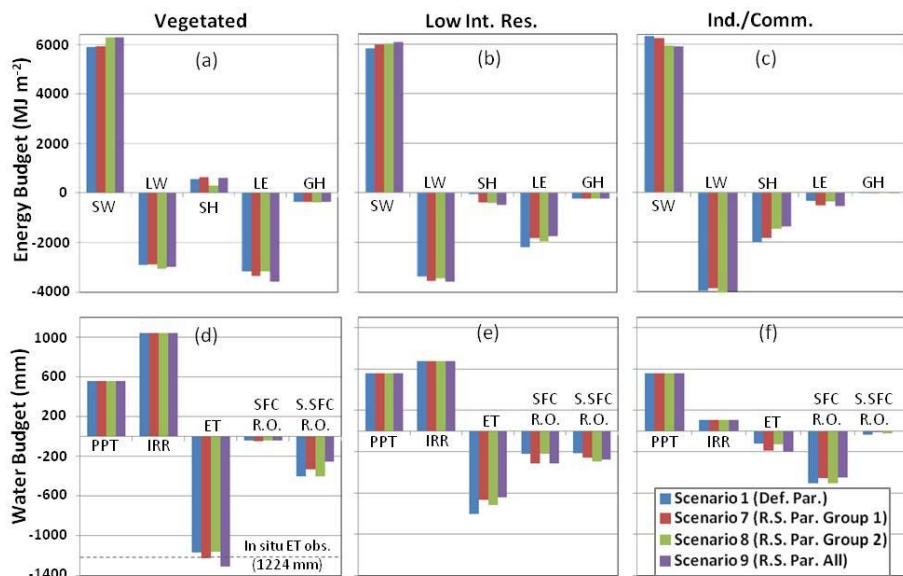
1138

1139 **Figure 6.** Noah/UCM simulated LST maps using different urban surface parameterizations: scenarios 1, 7, 8, and  
 1140 9 from Table 1 (top row) as well as differences between simulated and observed land surface temperature at  
 1141 1100 LST on 14 April 2011 (bottom row).

Deleted:

Deleted: 6

1142



1147

1148 **Figure 7. Differences in simulated energy (top) and water (bottom) budgets for WY 2011, using different urban**  
 1149 **surface parameterization and averaged over different land cover types. Energy budget terms include: shortwave**  
 1150 **radiation (SW), longwave radiation (LW), and sensible (SH), latent (LH), and ground (GH) heat fluxes. Water**  
 1151 **budget terms include: precipitation (PPT), irrigation water (IRR), evapotranspiration (ET), surface runoff (SFC**  
 1152 **R.O.), and sub-surface runoff (S.SFC R.O.).**

1153

1154

1155

1156

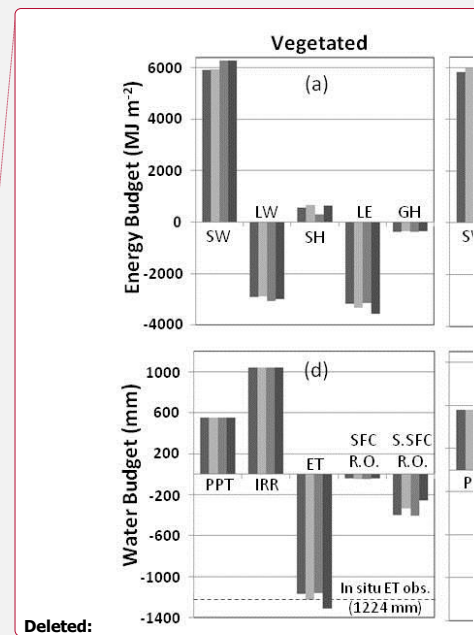
1157

1158

1159

1160

1161



1163

1164

1165

**Table 1. Model scenarios (1-9) and the incorporated remotely sensed parameter sets.**

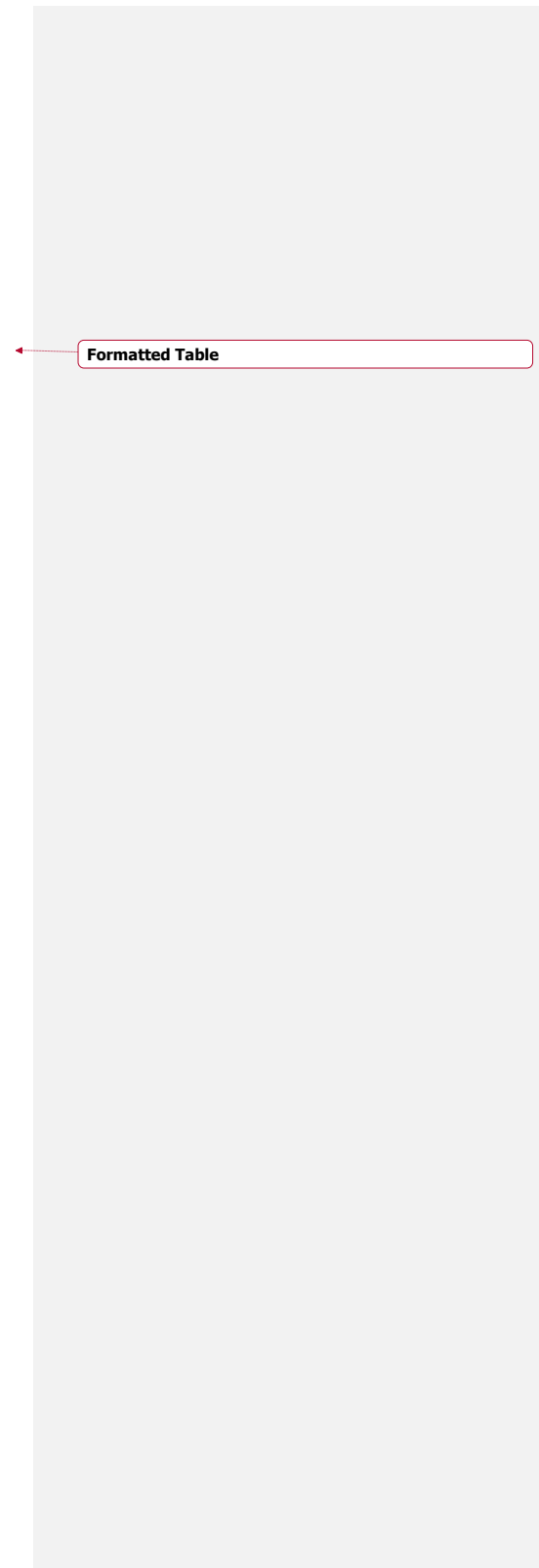
	GVF	ISA	Albedo	LAI	Emissivity
Scenario 1 (Def. Par.)	-	-	-	-	-
Scenario 2 (R.S. GVF)	X	-	-	-	-
Scenario 3 (R.S. ISA)	-	X	-	-	-
Scenario 4 (R.S. Albedo)	-	-	X	-	-
Scenario 5 (R.S. LAI)	-	-	-	X	-
Scenario 6 (R.S. Emissivity)	-	-	-	-	X
Scenario 7 (R.S. Par. Group 1)	X	X	-	-	-
Scenario 8 (R.S. Par. Group 2)	-	-	X	X	X
Scenario 9 (R.S. Par. All)	X	X	X	X	X

1166

1167

1168

1169



Formatted Table